Nanomed. J. 12:1 -, 2025

RESEARCH PAPER

In-vitro Anti-cancer and Antioxidant Activity of Biogenically Synthesized Co_3O_4@NiO Core-shell Nanostructures

Gezahegn Tadesse Ayanie*[1], Tegene Desalegn Zeleke[1], H.C Ananda Murthy[2], Lemma Teshome Tifa[1], Addisalem Abebe Godana[3]

[1]Applied Chemistry, Applied and Natural Science, Adama Science and Technology University, Adama, Ethiopia
[2] Department of Applied Sciences, Papua New Guinea University of Technology, Lae, Morobe Province, 411, Papua New Guinea, India
[3]Research Scholar, School of Chemical Sciences, Indian Institute of Technology Mandi, (IIT Mandi) Himachal Pradesh-175005, India

ABSTRACT

The anticancer and antioxidant activities of *Datura stramonium* plant leaf extract mediated Co_3O_4 and NiO nanoparticles, as well as Co_3O_4@NiO core-shell nanostructures were investigated. The Co_3O_4@NiO CSNs were synthesized with core-shell concentration ratios of 2:1, 1:1, and 2:3. The Co3O4@NiO CSNs and their parent nanoparticles were characterized by using advanced techniques. The band gap energy of Co_3O_4 (11) and NiO (11) NPs were found to be 3.06 eV and 3.45 eV, whereas, the band gap energies of the Co3O4 core and NiO shell were 3.68 and 4.52 eV, respectively. Similarly, the average crystalline size of Co_3O_4 (11) and NiO (11) NPs, as well as Co_3O_4@NiO (11) CSNs were found to be 18, 12, and 13 nm, respectively. The spherical shape of Co3O4, NiO NPs, and the spherical rod of Co3O4@NiO CSNs were investigated from SEM images. The particle sizes of cubic Co_3O_4, NiO NPs, and Co_3O_4@NiO CSNs obtained from TEM images were 15.55, 8.184, and 16.99 nm, respectively. The polycrystalline nature of CN was revealed from SAED analysis The percentage inhibition of Co_3O_4@NiO CSNs against MCF-7 cancer cells at 100, 200, 400, and 800 µg/mL were found to be 52.41, 68.21, 74.11, and 81.38%, respectively. The IC_{50} of Co_3O_4@NiO CSNs and epirubicin were found to be 21.25 and 18.01 µg/mL, respectively. The findings show that green synthesized Co_3O_4@NiO CSNs possess potential anticancer activities nearly comparable with standard drugs with less toxicity against normal cells.

Keywords: *Breast cancer, Anticancer; Antioxidant; Cytotoxicity*

How to cite this article
Ayanie GT, Zeleke TD, Murthy HCA, Tifa LT, Godana AA. In-vitro Anti-cancer and Antioxidant Activity of Biogenically Synthesized Co3O4@NiO Core-shell Nanostructures . Nanomed J. 2025; 12: 1-. DOI: 10.22038/nmj.2025.79882.1972

INTRODUCTION

Cancer and oxidative stress have recently been identified as the primary global health issues. Cancer, a non-communicable illness, is the second leading cause of mortality worldwide, behind cardiovascular disease. A cancer cell invades a healthy part of the body, changing biochemical and cellular functioning and eventually causing death [1, 2, 3, 4]. Breast cancer is mainly developed due to environmental and genetic factors. The report shows that about 27% of breast cancer is caused by genetic factors. Breast cancer is the most often diagnosed cancers that develop in the lining of the milk duct. Breast cancer became the most frequent class of fatal cancer in women throughout the world a few decades ago [5, 6]. The report showed the preferred prevalence rate for breast cancer increased from 16.7 to 33.6 per 100,000 women between 2000 and 2009. In 2014, the report showed about 232,670 new cases were detected and 40,000 women died in the USA. According to the most recent statistics from global research, the number of breast cancer patients in India will increase from 115,000 to 200,000 by 2030 [7]. Additionally, WHO reported that breast cancer caused 685,000 deaths and 2.26 million new cases in women globally in 2020 [8].

Several treatments have been developed to treat cancer- causing tumors, the most prevalent being surgery, radiation, immunotherapy,

---

* *Corresponding author: Email: sabkegezahegn@gamail.com*
Note. This manuscript was submitted on May 11, 2024; approved on August 26, 2024

biological, and chemotherapy [9, 10, 11]. However, these therapeutic approaches have severe side effects on normal cells, with limited effectiveness, toxicity, and non-selective towards cancer cells [12, 13, 14]. In breast cancer treatment, the type of chemotherapy used is typically determined by the tumor's unique receptor status. The primary receptors evaluated while choosing the proper chemotherapy treatment are hormone receptors (estrogen receptor (ER) and progesterone receptor (PR)), human epidermal growth factor receptor 2 (HER2), and triple-negative breast cancer (TNBC). Chemotherapy is frequently used in conjunction with targeted treatments of ER, PR, and HER2-positive breast cancer. However, chemotherapy remains the major systemic treatment option for triple-negative breast tumors, which have no targeted treatments. TBNC is a particularly difficult kind of breast cancer because it lacks the presence of the hormone receptor and HER2. This implies that TNBC does not react to targeted therapy. Chemotherapy intervenes in cell cycle control, suppresses proliferation, and has a cytotoxic impact, which causes intolerable side effects. Furthermore, this medication is ineffective against a wide variety of malignant tumors [15, 16, 17].

As a result, the researchers are interested in designing anticancer drugs that are non-toxic, selective, and effective. Cognizant of the promising effects of nanoparticles such as ZnO [18], Co_3O_4 [19], Fe_3O_4 [20] we explored the underlying mechanism through which iron oxide nanoparticles induce toxicity in human breast cancer cells (MCF-7, CuO [21], NiO [22], Si@NiO [4] researchers are interested in moving their attention from conventional medical techniques to the utilization of nanostructured materials for applying their atom-like behavior in anticancer therapy. The most notable of them are core-shell nanostructures, due to their important uses in drug administration, biomarkers, targeted therapy, and molecular imaging with minimal side effects in breast cancer treatment [23]. For example, ZnO-CuO nanoparticles inhibit breast cancer cell line (MCF-7) growth more than conventional drug doxorubicin at the same concentration [24].

In addition to cancer, the global population faces oxidative stress, which is caused by the overproduction of reactive oxygen species (ROS) in cells. In normal cellular metabolism, ROS such as superoxide radical (O_2^-), hydroxyl radical (OH^-), and hydrogen peroxide (H_2O_2) are formed as a byproduct that has a significant role in cell signaling and homeostasis [25, 26] Environmental stressors such as high temperatures, drought, salt, chemo-toxicity, radiation, and microbial attack cause an excess of reactive oxygen species to be formed [25]despite extraordinary progress. So, new cancer treatment modalities are needed. Tumor-treating fields (TTFs).

To avoid oxidative damage, endogenous antioxidants such as superoxide dismutase, catalase, and peroxiredoxins scavenge ROS produced during normal cellular metabolism and because of external factors [26]. However, excessive ROS formation creates oxidative stress, which is an imbalance between ROS and antioxidants and causes chronic illnesses such as diabetes, cancer, cardiovascular, and neurological disorders [19, 27]. To address this health problem, researchers have taken the initiative to develop various potent antioxidants to prevent oxidative damage. Exogenous delivery of antioxidants holds promise to alleviate oxidative stress to regain the redox balance. Amongst, there exist reports of the developed metal oxide and their combination with their potent antioxidants. Among the commonly studied, metal oxide nanoparticles such as ZnO [28], CuO [19], Co_3O_4 [29], Fe_3O_4 [30], NiO [31] are reported to be efficient in scavenging reactive oxygen species. Although several studies have been conducted and encouraging findings have been obtained, the problem of treating cancer and oxidative stress has not yet been entirely solved. As a result, the struggle to develop the most effective and strong medications to address the aforementioned human health concerns continues. In recent developments, metal oxide core-shell nanostructures are favored in biomedical applications over monometallic oxide and metal oxide nanostructures due to their superior attributes including low toxicity, high solubility, thermal and chemical stability, minimal defects, biocompatibility, and enhanced permeability to specific target cells as highlighted in recent literature reports [32]. Metal oxide core-shell nanoparticles (MOCSNs) such as NiO@ZnO [33, 34], Co_3O_4@NiO [35], Fe_3O_4@Ag [32, 36] Co_3O_4@ZnO [37], CuO@ZnO [38], Co_3O_4@SiO_2 [39], and TiO_2@Co_3O_4 [32] have been synthesized by using different methods and for several applications. These metal oxide core-shell nanostructures are synthesized by chemical methods such as sol-gel, hydrothermal, sono-coprecipitation, solvothermal, emulsion polymerization, microemulsion polymerization, ultrasonic microwave, electrochemical, and electroless deposition [40, 41]. Chemical methods are often expensive and potentially hazardous to the environment and living organisms. Thus, it has become imperative to design green synthesis methods to quest for safe, eco-friendly, cost-effective, quick, easily accessible, highly stable, and biocompatible synthesis [42, 43]. Owing to their wide availability and ease of preparation, plant- based phytochemicals caught the center of focus in green synthesis.

Datura stramonium (D.stamonium) is commonly called Jimson weed and it has a wide range of secondary metabolites with strong pharmacological effects. Previous research has reported on the secondary metabolites of *D. stramonium*, including alkaloids, flavonoids, glycosides, terpenoids, tannins, and phenolic compounds [44, 45]. Apart from its therapeutic use, substances like scopolamine and hyoscyamine are recognized for their psychoactivator properties [46]. Additionally, *D. stramonium* plant leaf extract was utilized in the green production of several nanoparticles because of the reducing and stabilizing qualities of its phytochemical ingredients.

Co_3O_4 and NiO NPs are presently recognized as the next generation of anticancer and antioxidant agents due to their bioavailability, dispersibility, selectivity, low host toxicity, permeability, and high effectiveness. Moreover, the synergetic effect that might arise from the combination of these metal oxides also derives interest in designing core-shell type nanostructures. In addition, core-shell nanostructure based therapies are being investigated and designed for a variety of breast cancer subtypes, with the most promising outcomes shown in the treatment of triple-negative breast cancer (TNBC) [15].

In this work, the Co_3O_4@NiO (CN) CSNs with a Co_3O_4 core encapsulated by NiO shell were synthesized using *D. stramonium* leaf extract as a reducing and capping agent that gave distinct qualities and capabilities that are not found in the individual materials. In addition, the anticancer and antioxidant efficacy of *D. stramonium* leaf extract mediated CN CSNs has not yet been reported. Finally, the anticancer effect against MCF-7 (Michigan Cancer Foundation-7) breast cancer cell line and the antioxidant activity of the green synthesized Co_3O_4@NiO CSNS were studied.

MATERIALS AND METHODS

Chemicals and reagents

In this study, chemicals such as ethanol (99.9%, LabTech Chemicals), cobalt acetate hexahydrate ($Co(CH_3CO_2)_2.6H_2O$) (Sigma Aldrich), nickel acetate dihydrate ($Ni(CH_3CO_2)_2{\cdot}2H_2O$) (Sigma Aldrich), distilled water, 2,2-diphenyl-1-picrylhydrazyl (DPPH) (Sigma Aldrich), ascorbic acid (Sigma Aldrich), Epirubicin (Sigma Aldrich), sodium hydroxide (NaOH) (Sigma Aldrich), and dimethyl sulfoxide (DMSO Sigma-Aldrich) have been used for the synthesis of Co_3O_4 and NiO NPs as well as Co_3O_4@NiO CN CSNs and evaluation of their biological activities. The chemicals and reagents were of analytical grade and used without further purification.

Datura stramonium leaf extract preparation

The collected *D. Stramonium* plant leaf was washed using tap water. After washing, the leaf was rinsed with distilled water to remove any contaminant substances from the surface of the leaf. The cleaned plant leaves were dried under the shed for 15 days and then ground using a grinding machine. During the extraction, the powder of *D. stramonium* leaves was mixed with 500 mL of distilled water in a 1000 mL conical flask. The mixture was boiled at 40 using a hotplate and stirred for 90 min. The extract was cooled to room temperature and filtered using Whatman Number 1 filter paper. Then afterward, the filtrate was collected and stored in the refrigerator at 4 °C.

Synthesis of cobalt oxide and nickel oxide nanoparticles

The cobalt oxide nanoparticles (Co_3O_4 NPs) were synthesized in a 1000 mL beaker in 1:2, 1:1, and 2:1 ratios of 0.5 M cobalt acetate hexahydrate and *D. stramonium* leaf extract, respectively, as shown in Fig. 1. For the synthesis of cobalt nanoparticles, the extract of the *D. stramonium* was added dropwise to 0.5 M aqueous solution of cobalt acetate hexahydrate followed by constant stirring for 4 h. Then, 0.1 M of NaOH was added and stirred for an additional 30 min to adjust the pH of the solution and enhance the formation of precipitate. The resulting precipitate was centrifuged at 4,000 rpm for 20 min to obtain Co_3O_4 NP precipitate. The sample was thoroughly washed with ethanol and distilled water to remove

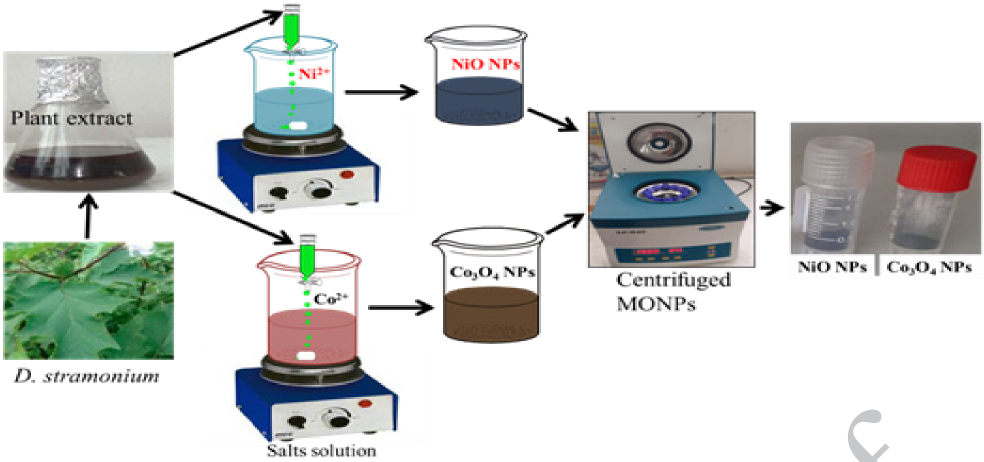

Fig. 1. Schematic procedure for the biogenic synthesis of Co3O4 and NiO NPs utilizing D. stramonium leaf extract

unwanted substances from the formed precipitate. The synthesized cobalt oxide nanoparticles were collected on the ceramic crucible and dried in an oven at 100 °C overnight and then allowed to cool. The same procedure was repeated for nickel oxide nanoparticles (NiO NPs) synthesis using the extract solution of the same plant leaf. The synthesized nanoparticles were stored safely for further analysis [47]

Synthesis of Co3O4@NiO CSNs

Cobalt acetate hexahydrate ($Co(CH_3CO_2)_2.6H_2O$) and nickel acetate dihydrate ($Ni(CH_3CO_2)_2.2H_2O$) precursor salts were utilized to synthesize CN CSNs. The CN CSNs were synthesized by holding the concentration of $Co(CH_3CO_2)_2.6H_2O$ constant (0.5 M) while varying the concentration of $Ni(CH_3CO_2)_2$.2H2O as 0.25, 0.5, and 0.75 denoted as CN21, CN11, and CN23, respectively, employing *D. stramonium* leaf extract as a reducing agent as shown in Fig. 2. Specifically in the synthesis of CN11, the *D. stramonium* leaf extract was gradually added to 0.5 M of $Co(CH_3CO_2)_2.6H_2O$ in a 1:1 volume ratio and stirred for 4 h. To adjust the pH of the mixture and enhance the precipitate formation, 0.1 M of NaOH was added and stirred for 30 min. Then to synthesize the CN CSNs, 0.5 M of $Ni(CH_3CO_2)_2.2H_2O$ about 100 mL was added and followed by the gradual addition of an equivalent volume of plant extract. The mixture was stirred for another 4 h. After the completion of stirring for 4 h, 0.1 M of NaOH was added to adjust the pH to 12 and stirred for 30 min. The precipitate was kept in a refrigerator for 12 h to enrich precipitate

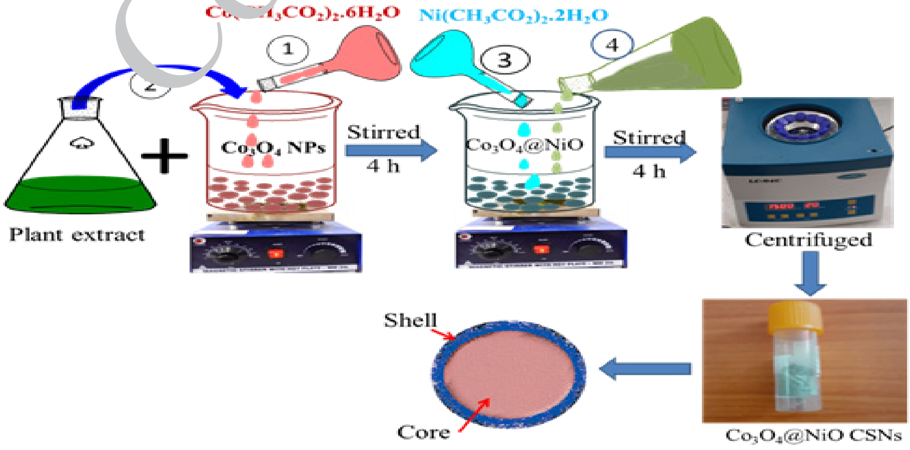

Fig. 2. The schematic route of the biogenic synthesis of CN CSNs

formation. Then, the synthesized Co_3O_4@NiO CSNs were washed three times using distilled water and ethanol. Finally, the precipitate was collected on the ceramic crucible and dried in the oven at 100 °C. The same procedures were repeated for the CN21 and CN23. The dried CN CSNs were calcined at 400 °C and kept for further analysis.

Characterization

Various characterization techniques were used to confirm the synthesis and properties of the metal oxides and the core-shell nanostructures. The thermal study of the Co_3O_4 NPs, NiO NPs, and CN CSNs has been done using the thermal gravimetric-differential thermal analysis (TGA-DAT (DTG-60H, SHI-MADZU Corporation, Japan)) in air flow heating rate of 10 ∕min starting at 30-800. To determine several functional groups, the green synthesized nanostructures were homogenized with a KBr pellet and analyzed using Fourier transform infrared spectroscopy (FT-IR) Bruker TENSOR27 spectrometer with a scanning range of 4000 - 400 cm^{-1}. The crystal structure and average crystallite size of Co_3O_4 NPs, NiO NPs, CN21, CN11, and CN23 nanoparticles were analyzed by using X-ray Diffraction (XRD-7000, SHIMADZU Corporation, Japan) furnished with a Cu metal used for generating a Cu Kα radiation with λ = 0.15406 nm and recorded in the range from 10-80. The scanning electron microscopy (SEM, model CamScan MV2300) was used to investigate the morphological structure of nanoparticles. Furthermore, the nanostructural properties of the nanoparticles have been elucidated by using a transmission electron microscope (TEM), higher transmission electron microscope (HRTEM), and selective area electron diffraction (SAED) model Philips CM30) functioned in 200 kV.

Anticancer activities

Breast cancer (MCF-7) and peripheral blood mononuclear (PBM) cells were acquired from India's National Center for Cell Sciences (NCCS). The breast cancer cells were cultivated using the standard technique of Dulbecco's Modified Eagle's Medium supplemented with fetal bovine serum. MCF-7 and PBM cells were bathed and grown in a humidified incubator at 37 °C in 5% CO_2 and injected with 10% (v/v) fetal bovine serum (FBS), penicillin (100 IU/mL), and streptomycin (100 g/mL) until they reached confluence. The cell was separated using a cell-dissociating solution (0.2% trypsin, 0.02% EDTA, and 0.05% glucose in PBS). After verifying the cells' vitality, they were centrifuged. In a 96-well plate, 5 × 104 cells/well were cultured and incubated for 24 h at 37 °C with 5% CO_2 [3].

The cytotoxicity of CN CSNs and Epirubicin on PBM and MCF-7 cells was determined *in vitro* using the 3-(4,5-dimethylthiazol-2-yl)-2, 5-diphenyltetrazolium bromide (MTT) assay [5]. The standard cells were trypsinized and adjusted to 5 × 104 cells/ml for cell counting in medium with 10% FBS (v/v). Each of the 96 wells of the µL plate received 100 µL of diluted cell suspension (5 × 104 cells/well). Following incubation, the test solutions in the wells were discarded, and 0.05 mg MTT was applied to each well. The plates were held for 4 h at 37 °C under a 5% CO_2 environment. The consequential formazan was dissolved in 100 µL of DMSO with moderate shaking at 37 °C. The absorbance was measured at 570 nm with a microplate reader. Equation (1) was used to calculate % growth inhibition, and dose-response curves for each cell line were utilized to get IC_{50} values [10]. Cell growth inhibitions were measured in triplicate and reported as mean ± standard deviation.

$$\%\text{Inhibition} = \frac{OD\ of\ control - OD\ of\ samle}{OD\ of\ control} * 100$$

(1)

The OD of control represents the optical density of the untreated control, whereas the OD of the sample represents the optical density of the treated sample, which is treated. The percentage inhibition was quantified by determining the difference between optical density between the control and the sample.

Antioxidant activities

The 2,2-diphenyl-1-picrylhydrazyl (DPPH) free radical was used to test the radical scavenging capacity of biogenically produced Co3O4 and NiO NPs as well as CN CSNs. The activity was assessed using the modified approach described in the earlier work report [27]. In DSMO, 3 mL of 100 µM DPPH was added to 1000 µL of methanolic Co3O4 and NiO NPs, as well as CN CSNs at concentrations of 50, 100, 200, 300, and 500 µg/mL. After sonication, the mixture was maintained in a dark chamber for 30 min before being incubated at 37±2 °C for the same amount of time. The UV-vis absorbance (UV-Vis) of the same concentration a positive control (ascorbic acid), Co3O4, NiO NPs as well as CN CSNs mixed with 0.1 mM DPPH was measured at at λmax of 517 nm. All the studies were carried out in triplicate, and the average absorbance for each sample was taken into consideration. Finally, the % scavenging capacity of nanoparticles was calculated using equation (2) [48].

$$\%\text{Radical scavenging activity} = \frac{\text{Absorbance of control} - \text{Absorbance of samle}}{\text{Absorbance of control}} * 100 \qquad \textbf{(2)}$$

Statistical data analysis

The experimental data were evaluated by using a statistical method known as the analysis of variance (ANOVA) function of the statistical package for social science (SPSS) version 20 and provided as a for triplicate experiments. Advanced software such as ImageJ (153-win imagej.exe), GatanMicroscopy Suite (GMS 64 bit), Origin software (Originpro 64 bit), and Microsoft Excel, 2013.

RESULTS AND DISCUSSIONS

As reported in our previous work, the phytochemical constituents of *D. stramonium* plant leaf, such as alkaloids, flavonoids, tannins, saponins, phenols, phytosterols, glycosides, terpenoids, and anthraquinones, were qualitatively screened. The phytochemicals containing hydroxyl and carboxy group were thought to be employed to decrease the size of the metal ion and cap the synthesized nanoparticles [49].

The CN CSNs were synthesized in two steps utilizing the *D. Stramonium* leaf extract from $Co(CH_3CO_2)_2.6H_2O$ which was used as a core and $Ni(CH_3CO_2)_2{\cdot}2H2O$ precursor salts as a shell in the nanostructures. The precursor salt of the core was mixed with the shell in (2:1), (1:1), and (2:3) concentration ratios. The synthesized Co_3O_4 core was coated with a NiO shell. The Ni2+ ions were electrostatically bound to the functional group of phytochemicals found on the surface of the core and possess reduction to some extent. The complete reduction of the shell was carried out after further addition of plant extract. The synthesized CSNs were capped and stabilized by these bioactive molecules as shown in Fig. 3. In the green synthesis of MONPs, the mechanistic electron interaction occurs in different stages. Under the controlled temperature and pH, the phytochemicals from the extract donate electrons to reduce metal ions to metal nanoparticles. Functional groups found in phytochemicals, including hydroxyl (-OH), carboxyl (-COOH), amino (-NH2), and others, can adsorb onto the surface of nanoparticles, giving stability and influencing the size and form of the particles. The metal ions are saturated to form hydroxyl complexes and grow up to form crystallite with oxygen after supersaturation as depicted in Fig. 3. The phytochemicals of *D. Stramonium* were used as a capping agent to stabilize the metal nanoparticles by preventing agglomeration [50, 51].

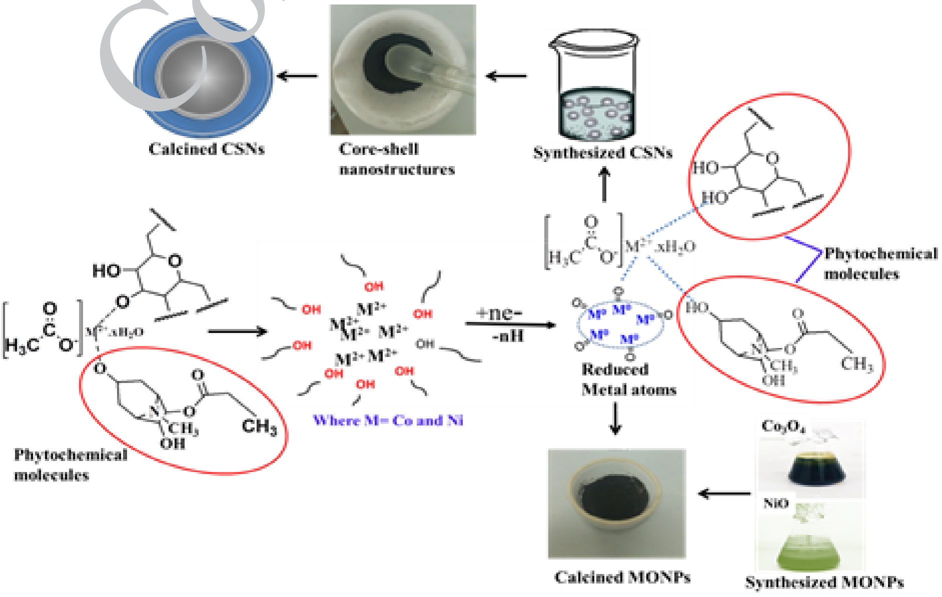

Fig. 3. Mechanism of green synthesis of metal oxide nanoparticles and core-shell nanostructures

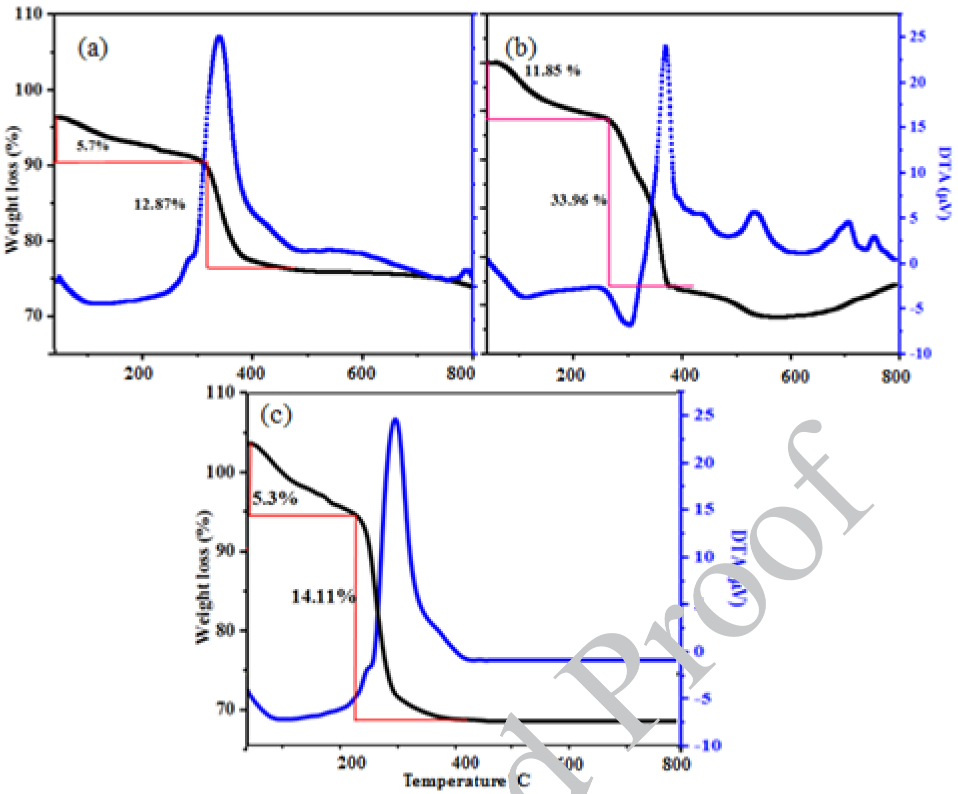

Fig. 4. The graph of TGA/DTA curve (a) Co3O4 NPs, (b) NiO NPs, and (c) Co3O4@NiO core-shell nanostructures.

Thermal analysis

The thermal stability of biogenically synthesized Co_3O_4, NiO, and CN CSNs was studied by using the thermogravimetric/differential thermal (TGA/DTA) analysis technique in an atmosphere through the speed of 10 at a temperature range of 30-800 as shown in Fig. 4. In TGA analysis the curve for Co_3O_4, NiO, and CN CSNs showed weight loss at two stages. The first weight loss of about 5.7%, 11.85%, and 5.3% in the range of 30-260, 30-260, and 30-220 were found to be water for Co_3O_4, NiO, and CN CSNs, respectively. The loss observed in the second stage was due to the decomposition of some organic molecules from the plant extract utilized during the synthesis of nanoparticles. The percent loss for these organic molecules was found to be 12.87%, 33.96%, and 14.14%, for Co_3O_4, NiO, and CN CSNs within the temperature ranges of 270-350, 270-380, and 230-400 , respectively.

Additionally, the exothermic and endothermic energy were also investigated by using differential thermal characterization techniques. The loss of weight and change in energy of synthesized samples indicated that the bioactive molecules involved in the synthesizing of nanoparticles were removed before calcination temperature. As shown in Fig. 4, the biologically synthesized Co3O4 NPs, NiO NPs, and CN CSNs became thermally stable at above 350, 380, and 400, respectively. These thermal points indicated that the calcination temperature of the synthesized sample was 350, 380, and 400 for Co_3O_4 NPs, NiO NPs, and CN CSNs, respectively.

UV-Vis analysis

The green synthesized Co_3O_4NPs, NiO NPs, and CN CSNs were analyzed by using UV-visible spectroscopy in the range of 200-800 nm wavelengths. As shown in Fig. 5, the absorption band of metal oxide nanoparticles synthesized in (1:1), (1:2), and (2:1) volume ratios and core-shell nanostructures denoted as CN21, CN11, and CN23 concentration ratios were recorded. The green synthesized nanoparticles absorbed light, which was recorded and utilized to calculate band gap energy. According to the generated data, the absorbance values for these nanoparticles differed mostly related to their size. Metal oxide nanoparticles absorb light of a given wavelength, causing electrons to move between the highest occupied and lowest empty orbitals.

As shown in Fig. 5(a), the absorption spectra of Co_3O_4 (11), Co_3O_4 (12), and Co_3O_4 (21) NPs developed bands at two distinct wavelengths. The absorption bands found at 230 and 276 nm were associated with Co_3O_4 (11) NPs, whereas 288 and 338 nm corresponded to Co_3O_4 (12), and 368 and 417 nm to Co_3O_4 (21) NPs, respectively. The absorption bands observed at shorter and longer wavelengths in each spectrum are caused by the charge transfer from $O^{2-} \rightarrow Co^{2+}$ and $O^{2-} \rightarrow Co^{3+}$, respectively [52]. Furthermore, the absorption spectra of NiO (11), NiO (12), and NiO (21) NPs were detected at 264, 296, and 310 nm, as shown in Fig. 5(b). All the absorption bands that occurred at 264, 296, and 310 nm were due to the charge transfer from O^{2-} to Ni^{2+} [53]magnetic hyperthermia constitutes a complementary way to cancer treatment. This article reports a promising aspect of magnetic hyperthermia addressing superparamagnetic and highly Fe/Au core-shell nanoparticles. Those nanoparticles were prepared using a wet chemical approach at room temperature. We found that the as-synthesized core shells assembled with spherical morphology, including face-centered-cubic Fe cores coated and Au shells. The high-resolution transmission microscope images (HRTEM. Among the Co_3O_4 and NiO NPs synthesized, the 2:1 ratios show λmax shift to the longer wavelength (red-shift). In contrast to the others, the energy level of Co_3O_4 (21) and NiO (21) NPs associated with their electronic states were changed and resulted in a plasmonic resonance shift. Similarly, the CN CSNs reflected the UV-visible light at two different wavelengths. As depicted in Fig. 5(c), the Co3O4-core and NiO-shell absorb the UV light at (254 nm, 322 nm), (240 nm, 306 nm), and (26 nm, 330 nm) pair of wavelengths that corresponds to electron transition between $O^{2-} \rightarrow Ni^{2+}$ within CN21, CN11, and CN23, respectively.

The absorbance data was utilized to derive the optical band gap energy of MONPs. The band gap energy was calculated using the Tauc relation, as stated in equation (3), [54] green synthesis of nickel oxide nanoparticles using phytochemicals from three different sources was employed to synthesize nickel oxide nanoparticles (NiOx NPs.

$$F(r)h\nu = A(h\nu - Eg)^2 \quad (3)$$

Where F(r) is the Kubelka-Munk function, is photon energy, and Eg is band gap energy. The

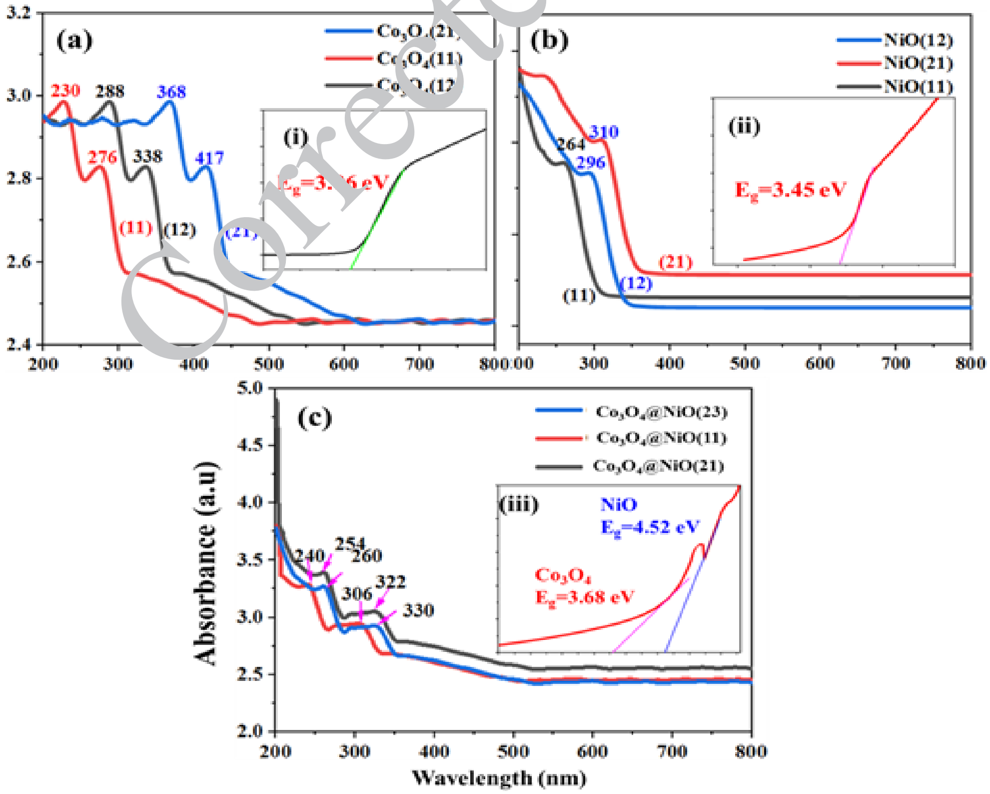

Fig. 5. UV-visible optical absorption spectra with their corresponding band gap energy of (a-i) Co3O4 NPs, (b-ii) NiO, and (c-iii) CN CSNs.

band gap energy values of all Co_3O_4 and NiO NPs and CN CSNs were calculated using extrapolation techniques. As shown in Figure 5(a-i and b-ii), the band gap of Co_3O_4 and NiO NPs was found to be 3.06 and 3.45 eV, respectively. In contrast to their corresponding bulk, the band gap value indicates a blue shift [55, 56]diffuse reflectance spectroscopy (DRS. The blue shift is because of the large band gap energy between the valance and conduction band in the nanoparticles. In general, the band gap energy of Co_3O_4 and NiO NPs was larger than their corresponding parent bulk materials [57].

The optical band gap energy of the green synthesized CN CSNs was also studied as shown in Fig. 5(c-iii). The Co_3O_4 core and NiO shell exhibit their characteristic band gap energy. According to Fig. 5(c-iii), the computed band gap energy values of 3.68 and 4.52 eV were believed to be associated with the Co3O4 core and NiO shell. The large band gap energy of NiO shell nanoparticles is in good agreement with UV-Vis data which has an inverse relation with absorption.

X-ray diffraction (XRD) analysis

The average crystallite size, the nature of crystal structure, and composition analysis of biogenically synthesized Co_3O_4, NiO NPs, and CN CSNs were examined using an XRD pattern. The diffraction pattern of Co_3O_4 NPs synthesized within three volume ratios such that 1:2, 1:1, and 2:1 were obtained from XRD analysis. The analysis was carried out using the X-ray photon (CuKα radiation) which is the energy released during the electron of k-shell return to its original state from the excited state at a characteristic wavelength of 0.154 nm and with the scanning rate of 0.16 s-1 within the range of 2θ from 10-80°. As depicted in Fig. 6(a), the diffraction peaks of Co3O4 NPs were observed for Bragg refraction with 2θ values of 19.02°, 31.22°, 36.82°, 38.[illegible]8°, 44.8°, 55.64°, 59.32°, 65.22°, and 77.26° corresponding to the set of lattice planes with Miller indices (hkl) values of (111), (220), (311), (222), (400), (422), (511), (440), and (622), respectively. Similarly, the diffraction peaks of green synthesized NiO NPs shown in Fig. 6(b) were obtained at 2θ values of 37.42°, 43.4[illegible]°, 63.06°, 75.56, and 79.58° matching with the miller indices of (111), (200), (220), (311), and (222) planes, respectively. The obtained result was complemented with the previous work and properly matched the standard database JCPDS card no. 00-042-1467 of Co3O4 NPs and 01-073-

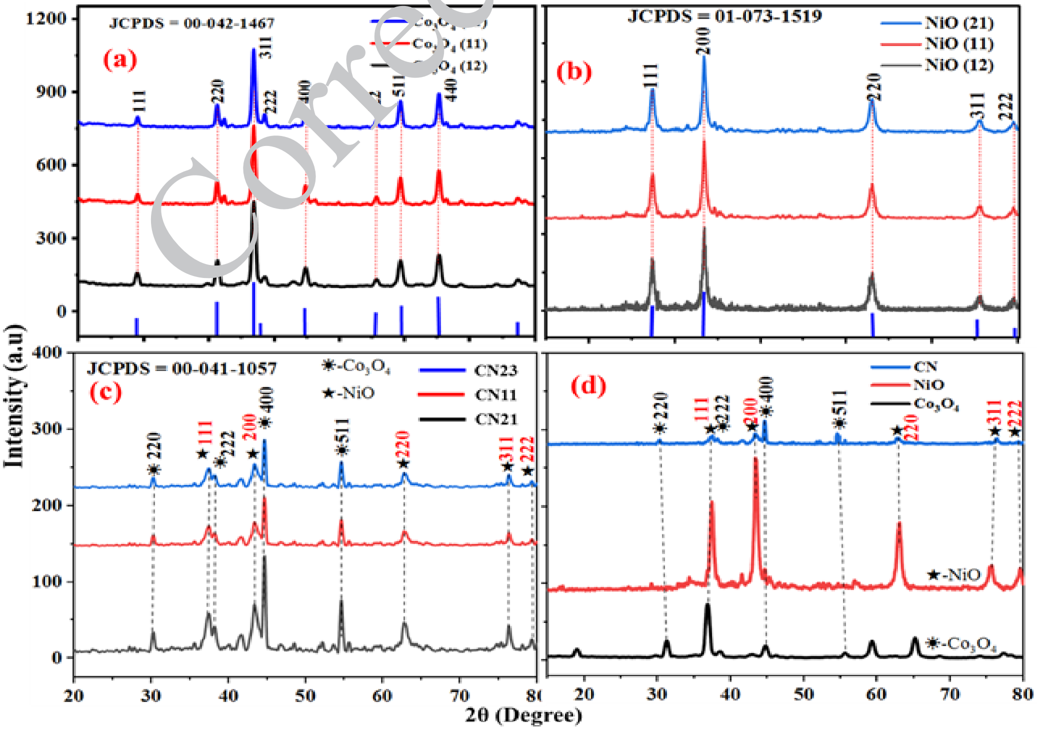

Fig. 6. The XRD pattern of (a) Co3O4 NPs, (b) NiO NPs, (c) CN CSNs, and (d) CN CSNs with parent nanoparticles

1519 of NiO NPs. The formation of core-shell nanostructure comprised of Co3O4 core and NiO shell NPs was also confirmed by using XRD analysis. As depicted in Fig. 6(c), the diffraction peak from the planes having the miller indices of (220), (111), (222), (200), (511), (220), (311), and (222) at 2θ values of 30.28, 37.52, 38.2, 43.32, 54.54, 62.72, 76.38, and 79.34°, respectively were obtained. The combination of plane lattice and diffraction patterns of CN CSNs indicated the formation of core and shell which agreed with the previous work [52]. Furthermore, the average crystalline sizes of biogenically synthesized Co3O4, NiO NPs, and CN CSNs were calculated using Debye-Scherrer's formula presented in equation (4) [58] green nanotechnology has gained attraction in the synthesis of metallic nanoparticles due to their cost-effectiveness, simple preparation steps, and environmentally-friendly. In the present study, copper oxide nanoparticles (CuO NPs

$$D = \frac{k\lambda}{\beta Cos\theta} \tag{4}$$

Where, *D* stands for average crystallite size (nm), *k* is the Scherrer constant (= 0.89 eV), is the wavelength of the X-ray photon (CuKα = 0.15406 nm), and β is the full-width at half-maximum (FWHM) of the diffraction peak appeared due to Braggs reflection in radian, and θ is half of the angle between transmission and diffraction. The calculated average crystalline size of Co3O4 NPs synthesized within volume ratios of (1:2), (1:1), and (2:1) were found to be 23, 18, and 21 nm, whereas, NiO NPs were 17, 12, and 15 nm, respectively.

XRD investigation revealed the cubic structure of Co3O4 NPs (space group Fd-3m). The length of cubic lattice parameters with a = b = c was determined. The estimated lattice parameter value was a = b = c = 0.8074012 nm, matching the theoretical value of 0.8072904 nm length with angles of α = β = γ = 90°. It was also found that NiO has a face-centered cubic structure with the space group 225: Fm-3m. In the crystal structure of NiO NPs, the lattice parameter was computed using equation (4) and found to be a=b=c=0.42024 nm with lattice angle (α = β = γ = 90°). The obtained lattice parameter values agreed with the theoretical 0.41268 nm.

Similarly, the average crystallite size of CN21, CN11, and CN23 were found to be 14, 13, and 16 nm, respectively. Reasonably, the calculated average crystallite size of CN11 is smaller than the two ratios due to the optimum concentration and volume ratios of precursor salt to plant extract. In the case of CN23, the amount of bioactive molecules present in the extract was not enough to reduce the size and cap the nanoparticles which led to the agglomeration of the particles and resulted in large particle size. Whereas in CN21 the excess amount of phytochemicals present in the leaf extract is believed to reduce very small size which can undergo nucleation and agglomeration. The XRD pattern of green synthesized CN CSNs was in good agreement with the previous report [57] The peak position of CSNs appeared at the same 2θ of parent materials that conformed well with standard pattern data and previous work. Green-synthesized Co_3O_4@NiO core-shell nanostructures had lower grain sizes than the chemically synthesized nanostructures, which might be advantageous in terms of performance and applications [59]

As shown in Fig. 6(c), the plane of the core material diffracted the X-ray radiation from the planes (220), (222), (400), and (511) at 2θ values of 31.22, 36.82, 38.48, and 55.64°, and the shell with the miller indices (111), (200), (220), (311), and (222) at 2θ of 37.42°, 43.42°, 63.06°, 75.56, and 79.58°, respectively. The Diffraction peaks of the shell material are more in number than that of the core materials relative to the individual nanoparticles. This confirmed that the NiO NPs were formed on the surface of Co_3O_4 NPs as a shell as reported elsewhere in previous reports. As shown in Fig. 6(c), all the diffraction peaks of the biosynthesized CN CSNs within all concentration ratios have fitted the peak of corresponding parent particles [60]. In addition to this, the formation of all CN CSNs correctly matched the standard database JCPDS card no. 00-041-1057.

FT-IR spectral analysis

The functional groups of *D.stramonium* plant leaf extract involved in the synthesis of MONPs and CSNs were reported in our previous work [37]. The functional groups contained in the biogenically produced Co_3O_4, NiO NPs, and Co_3O_4@NiO CSNPs were examined using FTIR spectroscopy. The functional group analysis was done between 4000-300 cm^{-1}. The absorption spectra resulting from various vibrational and stretching chemical bonds were used to predict the nature of the

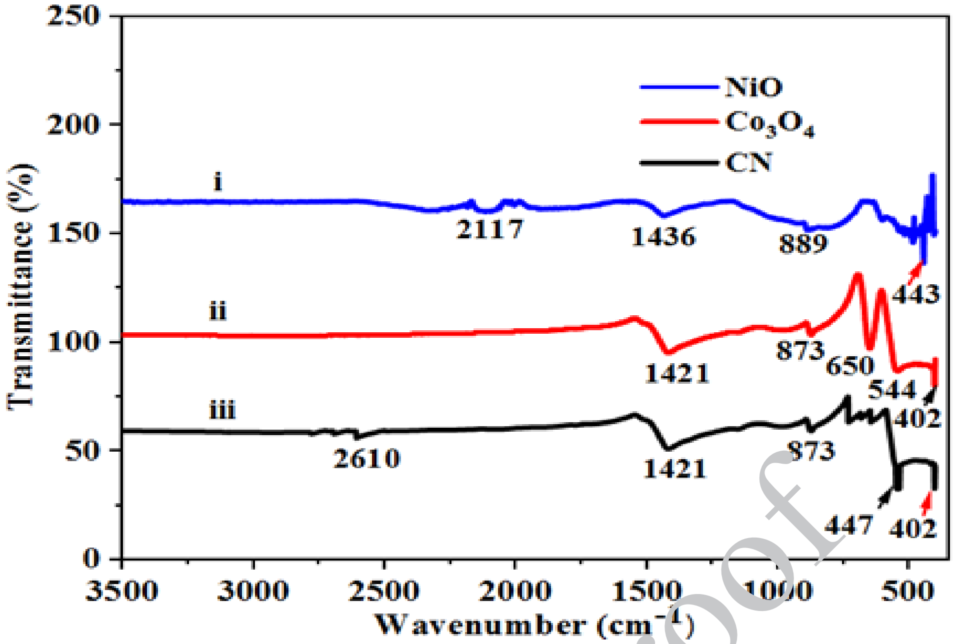

Fig. 7. FTIR spectra of D. stramonium leaf extract mediated (i) NiO NPs, (ii) Co3O4 NPs,, and (iii) CN CSNs.

synthesized nanoparticles. A variety of notable functional groups displayed absorption peaks at distinct wave numbers (cm^{-1}) in green-synthesized Co3O4 NPs.

The Co_3O_4 NPs exhibited two sequential stretching vibrations. Co_3O_4 NPs have two mixed valences: Co^{2+} and Co^{3+} ions, which produce O-Co^{2+} and O-Co^{3+}, respectively. The tetrahedrally coordinated Co2+ and octahedrally coordinated Co^{3+} ions stretched at 544 and 402 cm^{-1}, respectively. Because of nanoparticles' enormous surface area, CO2 molecules may be absorbed and form intermolecular interactions; causing the two more spectra formation within Co_3O_4NPs. The adsorbed CO_2 molecules undergo two characteristic bending vibration modes. As indicated in Fig. 7(ii) of Co3O4 NPs spectra, CO2 molecules exhibit in-plane bending vibration at 1421 cm^{-1} and out-of-plane bending vibration at 873 cm^{-1} [56]diffuse reflectance spectroscopy (DRS.

At the higher absorption wave numbers, the absence of peaks indicates that the green synthesized sample was calcined, causing the bioactive molecules to decompose. Similarly, the typical absorption peaks of NiO NPs of C-N stretching, asymmetric carbonate (CO_3^{-2}), and symmetric carbonate (CO_3^{-2}, were found to be 2117, 1436, and 889 cm^{-1}, respectively. The metal-oxygen stretching vibration in Ni-O undergoes absorption of infra-red radiation at 443 cm^{-1} as shown in Fig. 7(i). In addition, the absorption peak of Co_3O_4@NiO CSNPs was studied. Fig. 7(iii) shows that the absorption bands for Co_3O_4@NiO CSNPs were at 2610, 1421, 873, 447, and 402 cm^{-1} due to the C=O stretching of carboxylic acid, C-H bending, C=O of symmetric carbonate (CO_3^{-2}), Ni-O stretching vibrational, and Co-O vibration, respectively.

SEM-EDAX analysis

The surface topography of the green synthesized Co3O4, NiO NPs, and CN CSNs was revealed by using a surface morphology analyzer known as the scanning electron microscope technique. The surface of the Co_3O_4 NPs sample was scanned by an electron beam from a SEM instrument's electron gun, resulting in a nearly spherical and flattened shape, as shown in Fig. 8(a). The flattened surface of Co_3O_4 NPs is believed to be due to the agglomeration of the particles which leads to the enlargement of particles in size. ImageJ software was used to evaluate the particle size distribution of biologically synthesized Co_3O_4 NPs, revealing an average particle size of 63.4 nm in the 20-140 nm range as depicted in Fig. 8(d).

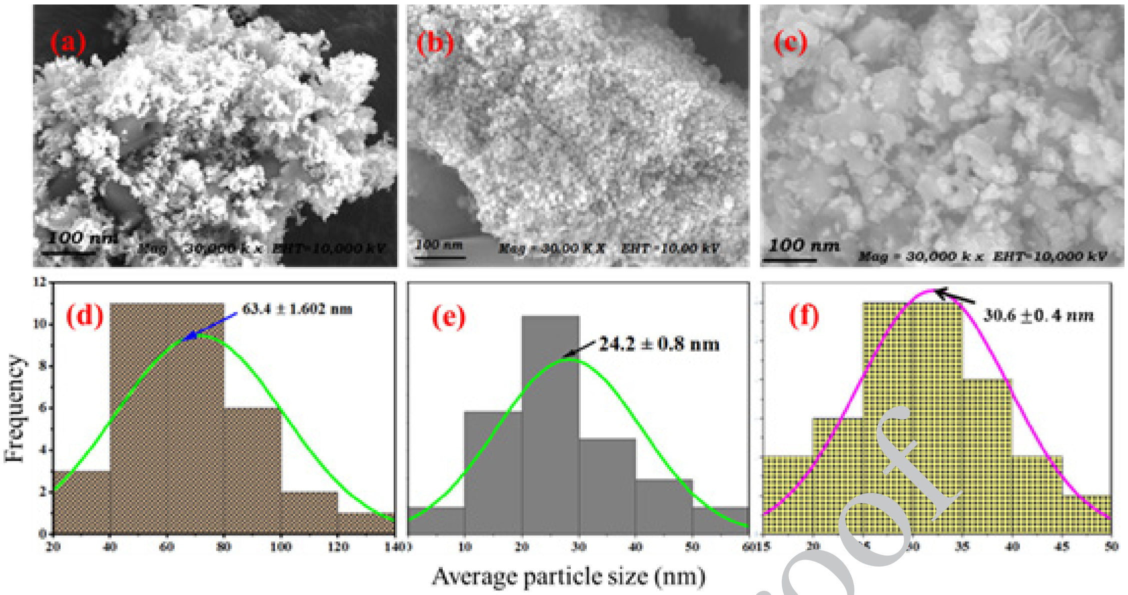

Fig. 8. The SEM images-particle size distribution (a/d) Co3O4, (b/e) NiO NPs, and (c/f) CN CSNs

Similarly, the morphological feature of NiO NPs was studied. Fig. 8(b) shows that the NiO NPs had a typical spherical form with a rough surface. Fig. 8(e) shows that NiO NPs have particle sizes ranging from 5 to 60 nm, with an average particle size of 24.2 nm. Similarly, SEM scans revealed the spherical and rod form of biologically synthesized CN CSNs, as illustrated in Fig. 8(c) [61] large specific surface area, simple preparation process, and convenient functionalization. In this study, a core–shell mesoporous material MCM-41@SiO2 was synthesized and functionalized by CoCl2, and subsequently KSCN, to prepare an ammonia adsorbent. The adsorbent was proved to possess high surface area, good sphericity, uniform size, good dispersibility, and high adsorption capability following DLS, SEM, TEM, and a static adsorption study. Moreover, the successful functionalization and thermal stability were confirmed by FT-IR, XPS, and TGA. The material was then used to fabricate a glass tube sensor for the rapid naked-eye detection of ammonia gas. The sensor showed good performance in terms of sensing speed, selectivity, accuracy, and reusability. Within 5 s, NH3 could be detected by the discoloration, and a wide NH3 concentration from 20 to 1000 ppm could be detected. It also showed a good linear relationship between discoloration length and ammonia concentration. A reversible color change from blue to yellow indicated the presence of NH3, which was attributed to the formation and disassembly of ammonia-containing complex [Co(NH3. The average particle size of CN CSNs has been found that 30.6 nm. In contrast to the average crystalline size obtained from XRD analysis, the particle size of Co_3O_4, NiO NPs, and CN CSNs calculated for SEM images was greater in small nanoscale. The larger average size of particles calculated for the SEM image indicated that particles were agglomerated to some extent.

The elemental composition of Co_3O_4 and NiO NPs was also investigated using energy dispersion X-ray spectroscopy (EDAX). As shown in Fig. 9(b), the 100% elemental composition of Co_3O_4 NPs confirms the existence of solely Co and O, ensuring that the synthesized nanoparticles are free from impurities. The elemental percentages of Co and O in Co_3O_4 NPs were determined to be 35 and 65%, respectively. The high-intensity peak suggests that green synthesized Co_3O_4 NPs have a higher percentage of oxygen. The elemental percentage of Ni and O in NiO NPs was found to be 66.3 and 33.7 %, respectively.

The elemental composition of Co_3O_4@NiO

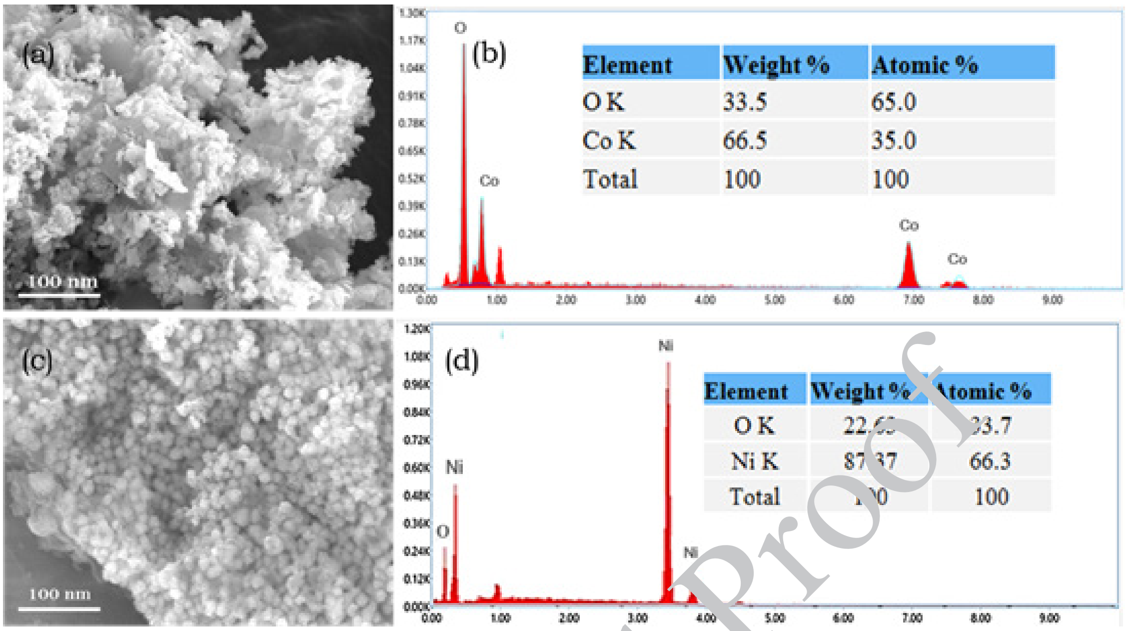

Element	Weight %	Atomic %
O K	33.5	65.0
Co K	66.5	35.0
Total	100	100

Element	Weight %	Atomic %
O K	22.63	33.7
Ni K	87.37	66.3
Total	100	100

Fig. 9. The SEM image-EDAX spectra of (a/b) Co3O4 NPs and (c/d) NiO NPs

CN CSNs was also identified and quantified using energy-dispersive X-ray (EDAX) techniques as depicted in Fig. 10. The distinctive peaks seen on the EDX graph demonstrate the successful synthesis of CN CSNs with desired elemental composition and no impurities. As shown in the graph of Fig. 10(e), all peaks represented the element belonging to the CN CSNs. The map sum spectrum of the sample also ensured that the green synthesized CN CSNs contained only O, Co, and Ni elements with atomic percentages of 60.48, 15.03, and 24.49%, respectively. Additionally, as depicted in Fig. 10(b) obtained from EDAX, the Co element with blue color is surrounded by the Ni element with green color which implies that Co_3O_4 NPs are found in the core and NiO NPs are on the shell which confirms the formation of Co_3O_4@NiO core-shell nanostructure and agreed with previous

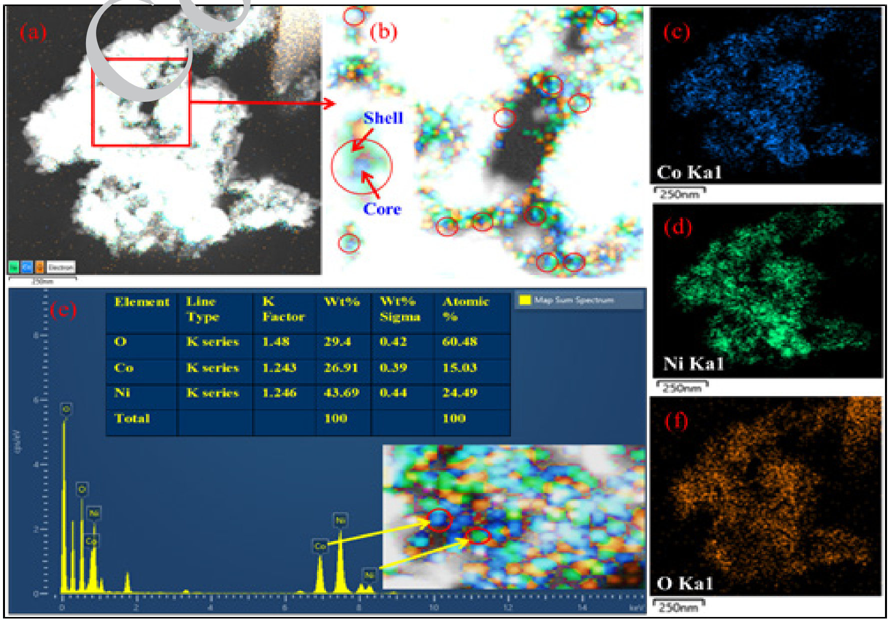

Element	Line Type	K Factor	Wt%	Wt% Sigma	Atomic %
O	K series	1.48	29.4	0.42	60.48
Co	K series	1.243	26.91	0.39	15.03
Ni	K series	1.246	43.69	0.44	24.49
Total			100		100

Fig. 10. The elemental composition of Co3O4@NiO core-shell nanostructure generated from EDX.

work [62].

TEM/HR-TEM and SAED analysis

The biologically synthesized Co_3O_4 and NiO NPs, as well as the CN CSNs, were further analyzed using TEM/HR-TEM and SAED methods. The TEM and HR-TEM images revealed precise information about the size, shape, and crystallinity of the MONPs and CSNs, while the SAED patterns confirmed the crystalline nature of the synthesized material. Fig. 11(a) shows that the *D. stramonium* plant leaf extract mediated Co3O4 NPs have cubic and rod shapes. Fig. 11(b) reveals the spherical and oval shapes of NiO NPs and the particle shapes are not evenly distributed, which is due in part to particle aggregation.

In addition to the mean particle size obtained from SEM Images and average crystalline size from XRD data, the mean particle size of Co_3O_4 and NiO NPs were also calculated from TEM images as shown in Fig. 11(c/d).

In the case of Co_3O_4 NPs, the particle size distribution was found to be between the 10-25 nm range, with a mean particle size of 15.55 nm as determined by the diameter of the particles measured using ImageJ software, as shown in Fig. 11(c).

Similarly, the average particle size of NiO NPs synthesized from plant leaf extract was evaluated. Fig. 11(d) shows that the particle sizes of NiO NPs were generally between 4-14 nm. The bioactive compounds stabilized the NiO NPs by establishing a protective layer and preventing aggregation, resulting in tiny size. Fig. 11(d) shows that the mean particle size of NiO NPs is 8.184 nm, with an uncertainty of ±1.64 nm. ImageJ software yielded an uncertainty of ±1.64 nm, indicating that NiO NPs varied in size from 6.54 to 9.82 nm.

The additional information related to the detailed morphological features of CN CSNs was investigated using TEM. The TEM images of CN CSNs presented in Fig. 12(a) showed a cubic and spherical shape. The shape of CN CSNs investigated from the TEM image is found to be in good agreement with the XRD data. As shown in Fig. 12(a) the darker area in the CN CSNs image is believed to be Co_3O_4 NPs which is a core and the lighter area shows NiO NPs which is a shell of synthesized particles. This finding is because of the difference in the electron sprinkling between

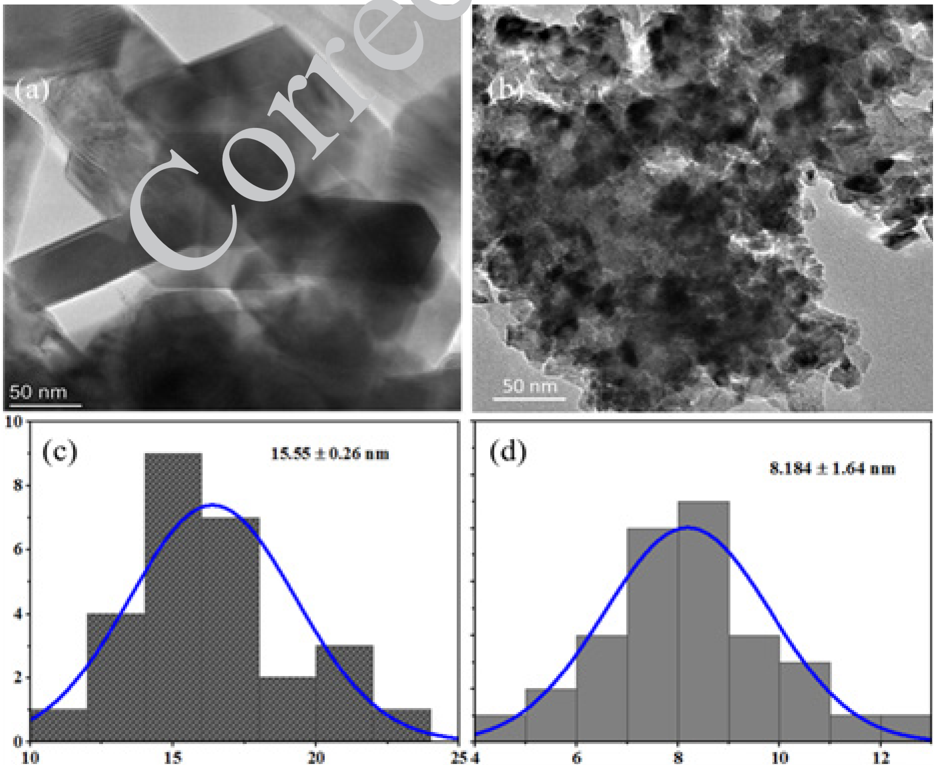

Fig. 11. The TEM image of (a) Co3O4 NPs, (b) NiO NPs, and Particle size distribution of (c) Co3O4 NPs and (d) NiO NPs

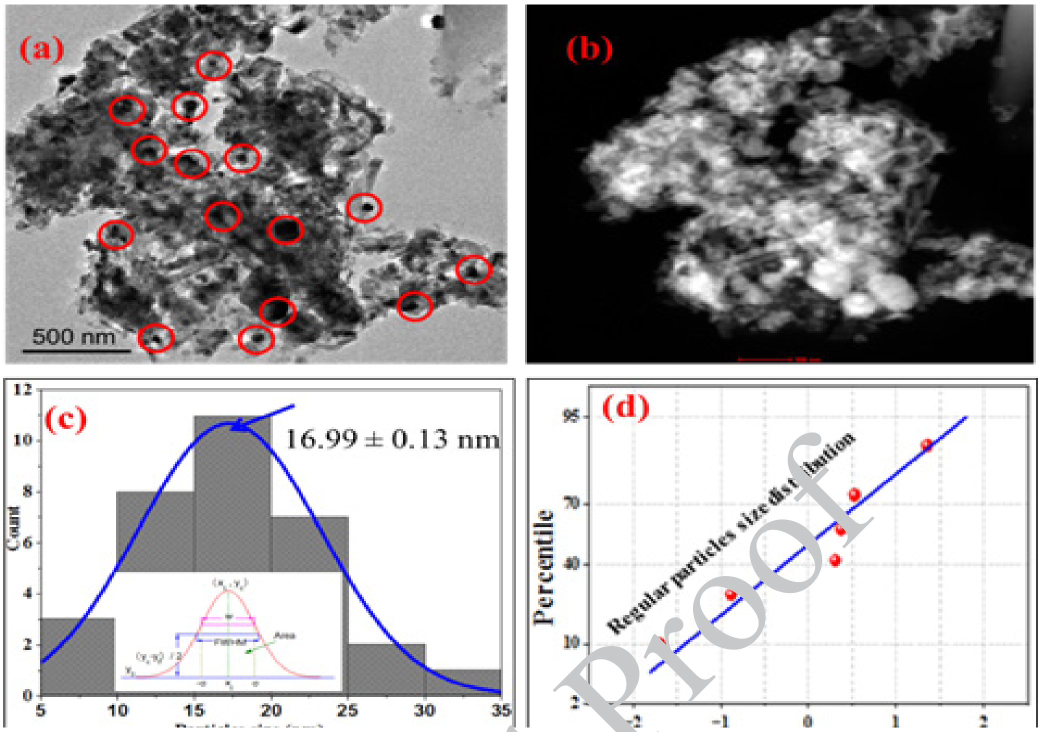

Fig. 12. The CN CSNs analyzed (a) TEM image, (b) STEM image, (c) particle size distribution and (d) regular particle size distributions.

the core and shell particles. Similarly, the scanning transmission electron microscope (STEM) image in Fig. 12(b) indicates the formation of CN CSNs in which the white region shows the high electron density of core and shell materials. The distribution of CN CSNs across the TEM image in terms of their size was also obtained.

The diameter of 60 particles was measured by using Gatan software and the mean particle size was determined from histogram. As depicted in Fig. 12(c) the mean particle size of CN CSNs was found to be 16.99 nm with a standard deviation of 0.13 nm. The range of particle size distribution was within 5-35 nm which implies that the CN CSNs were found to be agglomerated to some extent which might be attributed to the removal of bioactive molecules during calcination. The originally bioactive capped CN CSNs shrunk together after the calcination and resulted in agglomeration.

The grains and lattice fringe alignment of Co_3O_4NPs was evaluated using HR-TEM as depicted in Fig. 13(b). The structural fingerprints produced by incident electron diffraction after passing through the material were utilized to calculate the inter-planar distance. The distinctive distance between the fringes was obtained using the IFFT model

The inter-planar distance for Co_3O_4 NPs was determined to be 0.3286 nm, referring to the plane (311). Fig. 13(b) shows the strong visibility and long-range alignment of the structural fingerprinting, showing that the biologically produced Co3O4 NPs are single-crystalline for a specific range. The inter-planar distance for Co3O4 NPs was determined to be 0.26 nm, referring to the (311) plane.

Furthermore, the crystallinity of Co_3O_4 NPs was investigated using the SAED image displayed in Fig. 13(d). The parallel pattern is associated with electron diffraction by crystal lattice planes. The alignment and brightness of these parallelly organized dots reveal the configuration of atoms within the crystal. Thus, it implies that the atoms in biologically produced Co_3O_4 NPs are arranged consistently and have a single crystalline structure.

The crystal structure and lattice parameters of NiO NPs were examined using high-resolution TEM (HR-TEM). Fig.s 14(a) and 14(b) show the HR-TEM image and the space between the lattice

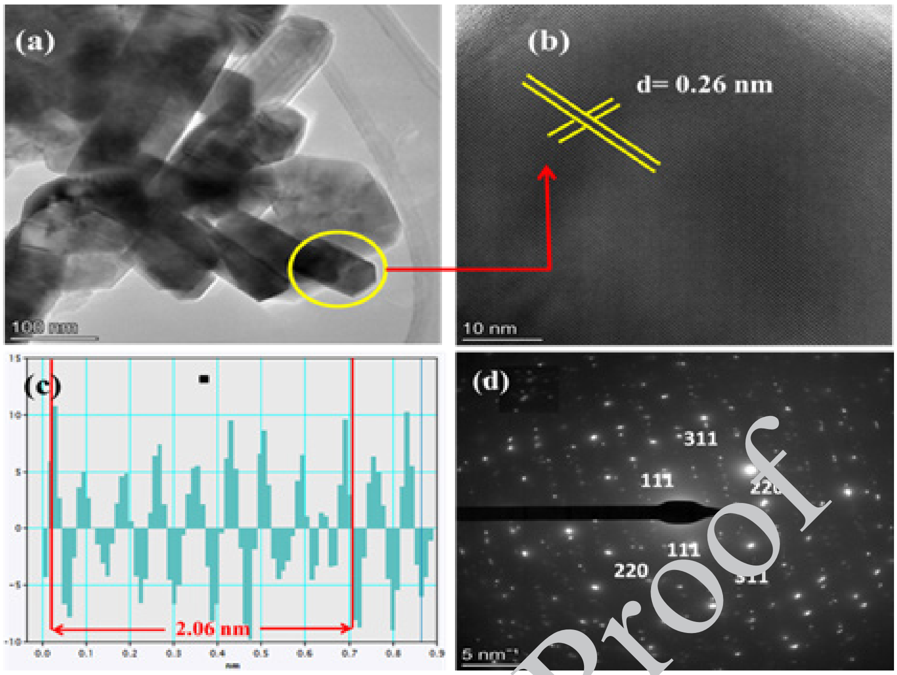

Fig. 13. The morphological images of Co3O4 NPs, (a) TEM image, (b) HR-TEM image, (c) inverted Fast fourier Fourier transform Transform (IFFT), and (d) SAED images

fringes. The d-spacing values shown in Fig. 14(b) were determined using Gatan software. The lattice distance for the respective miller indices (111) was determined to be 0.26 nm. The characteristic (hkl) values of NiO NPs with d-spacing values determined from SAED were in good agreement with the conventional XRD values.

Moreover, the crystal structure of the green synthesized NiO NPs was determined using SAED images shown in Fig. 14(d). The circular diffraction pattern was generated based on the particle orientation and size. The circular diffraction spot correlates to the crystal structure's lattice points with concentric rings, indicating that the produced NiO NPs are polycrystalline.

The CN CSNs containing Co_3O_4 core and NiO

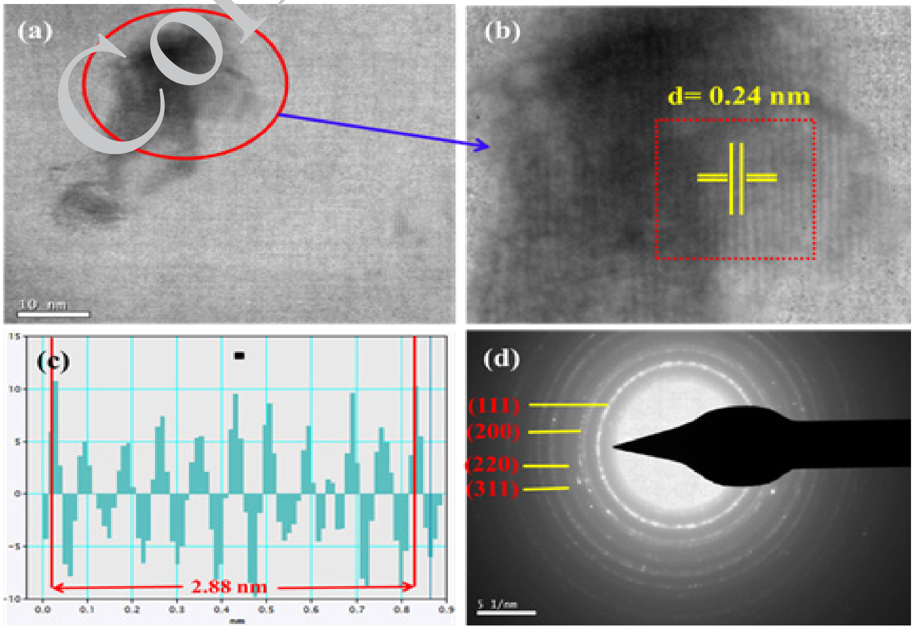

Fig. 14. The morphological images of NiO NPs, (a/b) HR-TEM image, (c) (IFFT), and (d) SAED images

shell were further examined by using HR-TEM. The core-shell structures, interface of core and shell, and the distance between adjacent crystals lattice planes in the nanostructure have been explored. In the analysis, the highly magnified CN CSNs showed the core and shell structure. As shown from the TEM image in Fig. 12(a), the HR-TEM image also showed the dark region that ensures the formation of the core and shell nanostructure. In the area where the NiO shell coats the Co_3O_4 core appeared darker in the HR-TEM image. The darker region is believed to be because of higher electron density in the core, resulting in different electron scattering. Under high-resolution detection with the beam of an electron, the incident electron from the electron gun passes through the core of the CN CSNs sample and experiences strong diffraction because of the high density of the electron. The strong diffraction causes a reduction in the intensity of the electron reaching the detector, resulting in a darker region in the HRTEM image. In contrast, the NiO shell with lower electron density diffracts electrons to some extent whereas most electrons reach the detection and result in brighter regions of the shell observed in Fig. 15 (a).

On the other hand, the shell material, which has a lower atomic number and electron density, scatters electrons to a lesser extent. As a result, more electrons reach the detector, leading to a brighter appearance in the image. The distance between adjacent crystal lattice planes of the Co_3O_4 core corresponding miller indices (400) was found to be 0.25 nm, which is presented in Fig. 15(b). Similarly, the d-spacing for the NiO shell with miller indices (111), (200), and (220) were 0.25, 0.21, and 0.13 nm respectively. The miller indices obtained from HR-TEM and SAED were found in good agreement with the d-spacing values of standard XRD data.

Moreover, Fig. 15(d) indicated that the SAED image of CN CSNs where miller indices are shown with their corresponding planes. The miller indices were identified from the d-spacing values of the crystal lattice planes of CN CSNs. The calculated lattice space belongs to the miller indices of CN CSNs which are used to confirm the formation of core-shell nanostructure. In addition, the SAED image explored the crystalline structure of green synthesized CN CSNs. As shown in Fig. 15(d), the

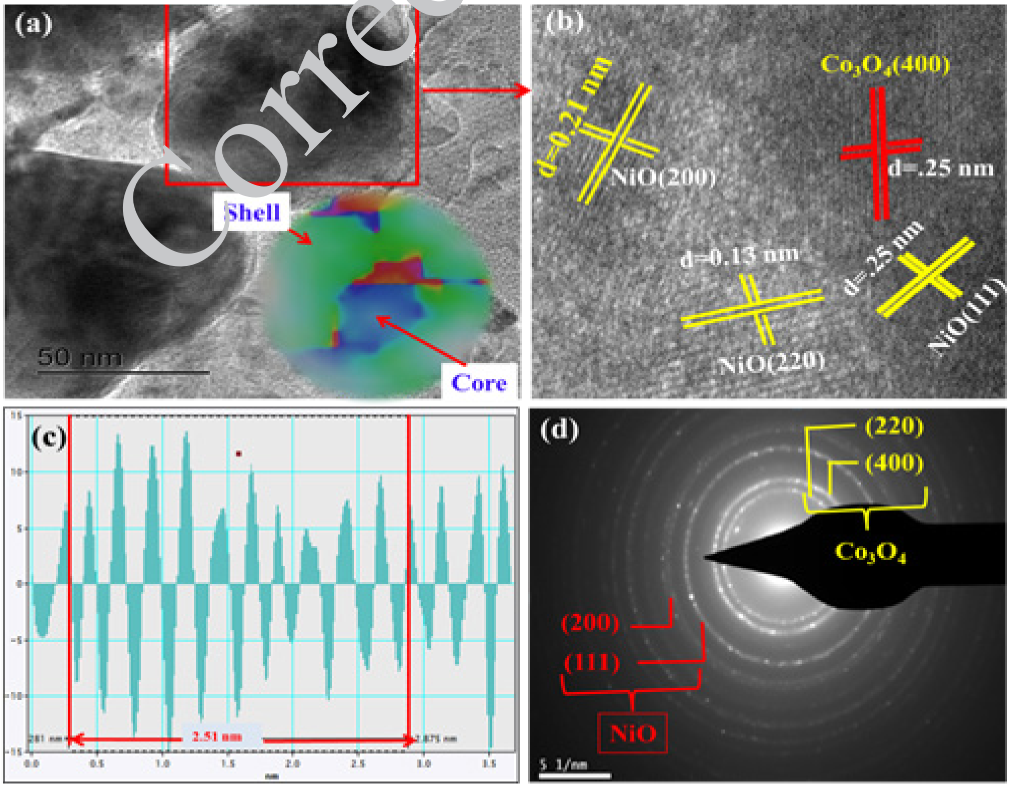

Fig. 15. Biologically synthesized Co3O4@NiO core-shell (a) HR-TEM, (b) d-spacing obtained from HR-TEM of particles, (c) IFFT, and (d) SAED images.

well-defined ring was revealed that shows the polycrystalline nature of CN CSNs. The nanowire Co3O4/NiO with 10 nm thickness of NiO shell was reported in another previous work [35]which requires a combination of high mass-loading and high utilization of electrochemically active material. In this work, we report the fabrication of hierarchical core-shell Co_3O_4@NiO nanowire@ nanorod arrays where ultrathin NiO nanorods (~5nm. The fringes with d spacing 0.46 nm correspond to the (111) lattice plane of Co3O4, whereas those at 0.24 nm correspond to the (111) lattice plane of NiO. HRTEM data show that Co3O4 coexists with NiO [59]. Similarly, the Co3O4@ NiO CSNs synthesized in the current study had d spacing of 0.36 nm, which could be associated with the (111) lattice plane of the Co_3O_4 core, and 0.25 nm for the NiO shell NPs. The reduced d-spacing of the core and the resulting lattice strain can affect the electrical structure and surface characteristics of nanostructures which could result in increased reactivity and performance in a variety of applications.

Anticancer activities result

The core-shell nanostructures have recently gained attention for their potential anticancer effects due to their biocompatibility, stability, and pharmacokinetics. The two most important conditions for breast cancer therapy are efficacy and selective toxicity. To address these issues, MONPs, the most promising alternative to traditional chemotherapy for breast cancer treatment, underwent comprehensive testing. Previous studies indicated that ZnO NPs killed 53.3% of MCF-7 cells at a dosage of 100 µg/mL, with an IC_{50} of 12.7 µg/mL (25). Furthermore, the anticancer properties of Fe_3O_4@ZnO NPs and their parent materials were investigated. Compared to the MONPs, core-shell NPs demonstrated a much stronger cytotoxic effect. This indicates that the properties of the cor-shell nanoparticles have altered, and they outperform single MONPs in all of their activities. Similarly, NiO NP shells were coated onto Co_3O_4 core NPs for breast cancer therapy in this research [63].

The cytotoxicity of CN CSNs, as well as Epirubicin (standard drug), was assessed against breast cancer (MCF-7) cell lines and peripheral blood mononuclear (PBM) cells using an MTT assay. In this work, different exponential concentrations of CN CSNs, as well as Epirubicin of 12.5, 25, 50, 100, 200, 400, and 800 µg/mL have been examined on MCF-7 and PBMC as shown in Fig. 16. In the case of CN CSNs, the in vitro cytotoxicity against MCF-7 cell lines and PBMC healthy cells was examined.

As depicted in Fig. 16, the images of MCF-7 cell lines treated with 100, 200, and 400 µg/mL of CN CSNs and standard drug were taken by using a fluorescence microscope (KFL30LED, India). To determine the cytotoxicity of CN CSNs against the cultured breast cancer cell lines, the micrograph was captured at the wavelength of 520 nm. Consequently, the white (live) and smooth non-white area (dead) cells were observed.

Fig. 17 and Table 1 indicate that CN CSNs inhibit

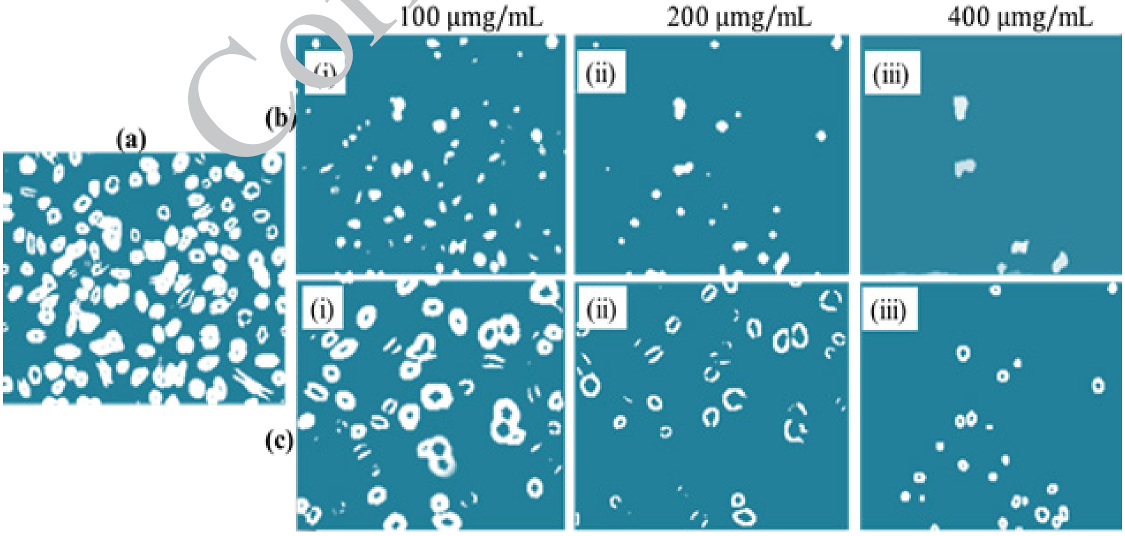

Fig. 16. Cytotoxicity on MCF-7 cell lines: (a) untreated, (b) treated with Epirubicin of 100 µg/mL(i), 200 µg/mL(ii), and 400 µg/mL (iii) and (c) treated with CN CSNs of 100 µg/mL(i), 200 µg/mL(ii), and 400 µg/mL (iii).

cancerous cells at 12.5, 25, 50, 100, 200, 400, and 800 µg/mL by about 22.16, 32.20, 43.62, 52.41, 68.21, 74.11, and 81.38%, whereas Epirubicin drug inhibits 33.42, 46.68, 55.31, 74.53, 81.22, 86.77, and 96.15%, respectively. The CN CSNs and Epirubicin have IC_{50} values of 73.89 and 15.08 on MFC-7, and 455.86 and 419.40 on PBMC. This suggests that D. stramonium leaf extract-mediated CN CSNs are as effective as conventional drugs in terms of anticancer activity while being less toxic to normal cells.

As shown in Fig. 16, the number of cells decreased as the concentration of CN CSNs against MCF-7 cell lines. The mechanistic biological contact of CN CSNs with MCF-7 may include endocytosis, in which $Co^{2/3+}$ and Ni2+ ions pass through the cell membrane. The tiny size and high surface charge of CN CSNs allow for powerful anticancer action. CN CSNs can produce reactive oxygen species, resulting in oxidative stress and cancer cell death. Elevated ROS levels in the cell can also promote DNA alteration and lesion, which can result in both double and single strand breaks. Table 1 reveals that CN CSNs exhibit substantial toxicity on MCF-7 cell lines, with an IC_{50} value of 73.89 µg/mL, indicating their potency as an anticancer agent.

Mechanistic Interaction of CSNs with Breast Cancer Cells

The objective of anticancer drugs is to prevent

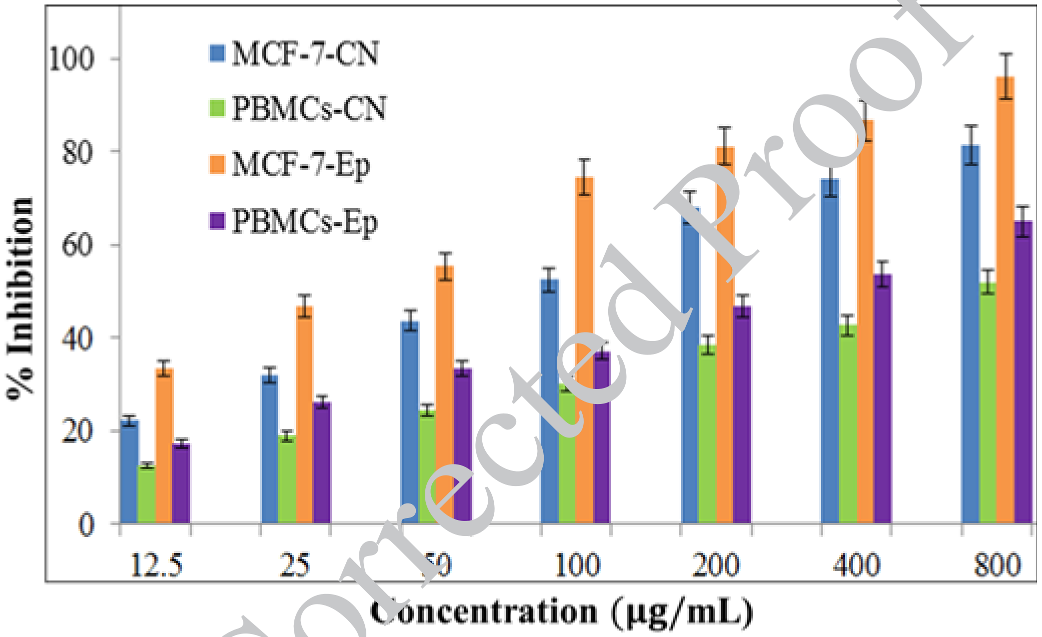

Fig. 17. Cytotoxicity of CN CSNs and Ep against PBM and MCF-7 cell lines

Table 1. The percentage inhibition of CN CSNs and Ep against PBM and MCF-7 cell lines at different concentrations.

Conc. (µg/mL)	Co_3O_4@NiO (% In)		Epirubicin (% In)	
	MCF-7	PBMCs	MCF-7	PBMCs
DMSO	0.00	0.00	0.00	0.00
12.5	22.16 ± 0.03	12.57 ± 0.02	33.42 ± 0.03	17.13 ± 0.01
25	32.20 ± 0.02	18.88 ± 0.02	46.68 ± 0.01	26.33 ± 0.03
50	43.62 ± 0.00	24.44 ± 0.01	55.31 ± 0.02	33.56 ± 0.02
100	52.41 ± 0.01	30.21 ± 0.01	74.53 ± 0.03	37.23 ± 0.00
200	68.21 ± 0.03	38.54 ± 0.03	81.22 ± 0.01	46.66 ± 0.03
400	74.11 ± 0.03	42.67 ± 0.04	86.77 ± 0.00	53.52 ± 0.02
800	81.38 ± 0.01	51.94 ± 0.02	96.15 ± 0.02	65.18 ± 0.04
IC_{50}	73.89	455.86	15.08	419.40

tumor cell growth and cause death without a significant negative impact on healthy cells. The specific molecular mechanisms involved in the interaction between nanoparticles and breast cancer cells can vary depending on the type of nanoparticle, its physicochemical properties, the breast cancer cell line, and the experimental conditions [64 65]. The CN CSNs having unique physicochemical features have emerged as a new hope for cancer therapy. By delivering drugs directly to cancer cells, anticancer treatment can be more effective while minimizing adverse effects. The CN CSNs inhibit and induce death by oxidative stress, causing DNA damage, arresting the cell cycle, and inducing cancer cell death by apoptosis as well as nonapoptotic modes of cell death.

In cancer cell proliferation, cyclin-dependent kinase 1/2 (CDK1/2) plays a crucial role in the whole cell cycle. It has become a new target for cancer therapy. CDK1interacts with cyclin B1 to facilitate the transition from the growth (G2) phase into mitosis, whereas CDK2 activates the growth 1/synthesis (G1/S) and synthesis/growth 2 (S/G2) transitions in the interphase stage of cell cycle. As shown in Fig. 18, the delivered metal ion of CN CSNs believed to inhibit the activity of CDKs by binding to groups such as imidazole nitrogen of histidine, amide nitrogen atoms of asparagine and glutamine, carboxylate oxygen atoms of aspartic acid and glutamic acid, hydroxyl oxygen atoms of serine, threonine, and tyrosine residues, and thiol group of cysteine amino acids. Similarly, particular elements inside DNA polymerase, such as the nitrogen, oxygen, and sulfur atoms of amino acids, reacted with metal ions found in CN CSNs, inhibiting its action. The other key mechanism of CSNs to induce the death to cancer cells is producing Reactive oxygen species (ROS). Once the the CN CSNs are internalized by the cancer cell through the endocytic pathway and dissolved into metal ions, and disrupts the cellular homeostasis. This homeostasis disruption, resulted in the production of excessive ROS within the cancer cells, leading to oxidative stress and mitochondrial dysfunction.

Additionally, the core-shell nanoparticles are recognized and taken up by the breast cancer cells through receptor-mediated endocytosis. Once the CN CSNs are internalized, they become entrapped within the endocytic vesicles, which then fuse with lysosomes to form endolysosomes as shown in Fig. 18. The CN CSNs is released into the cytoplasm once the endolysosomal membrane is disrupted,

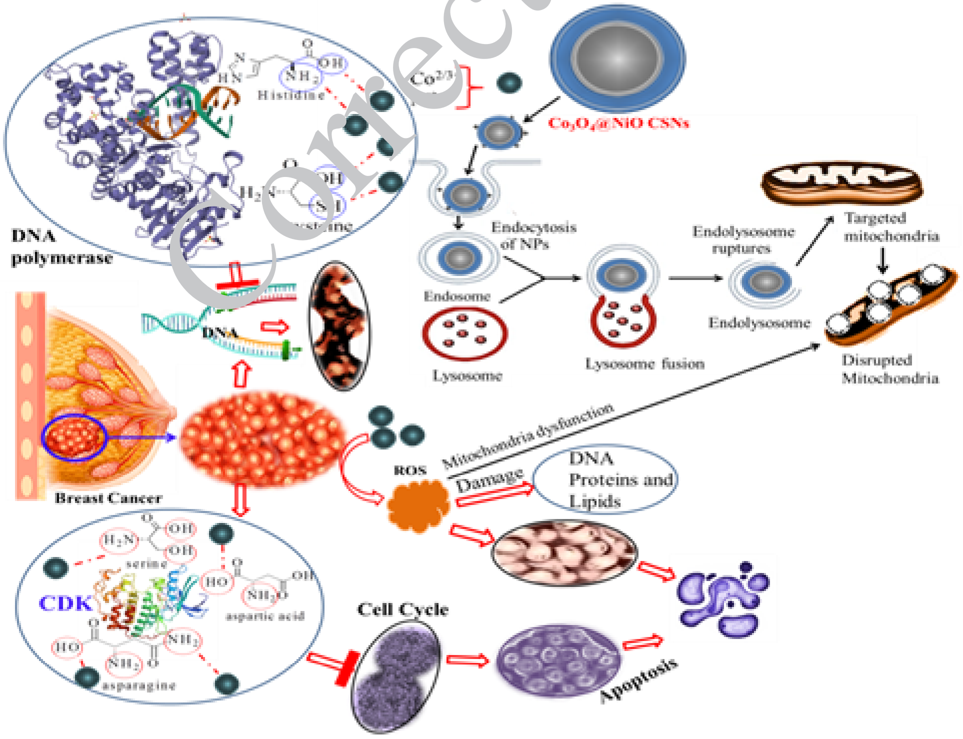

Fig. 18. Mechanistic interaction of CN CSNs with breast cancer cells

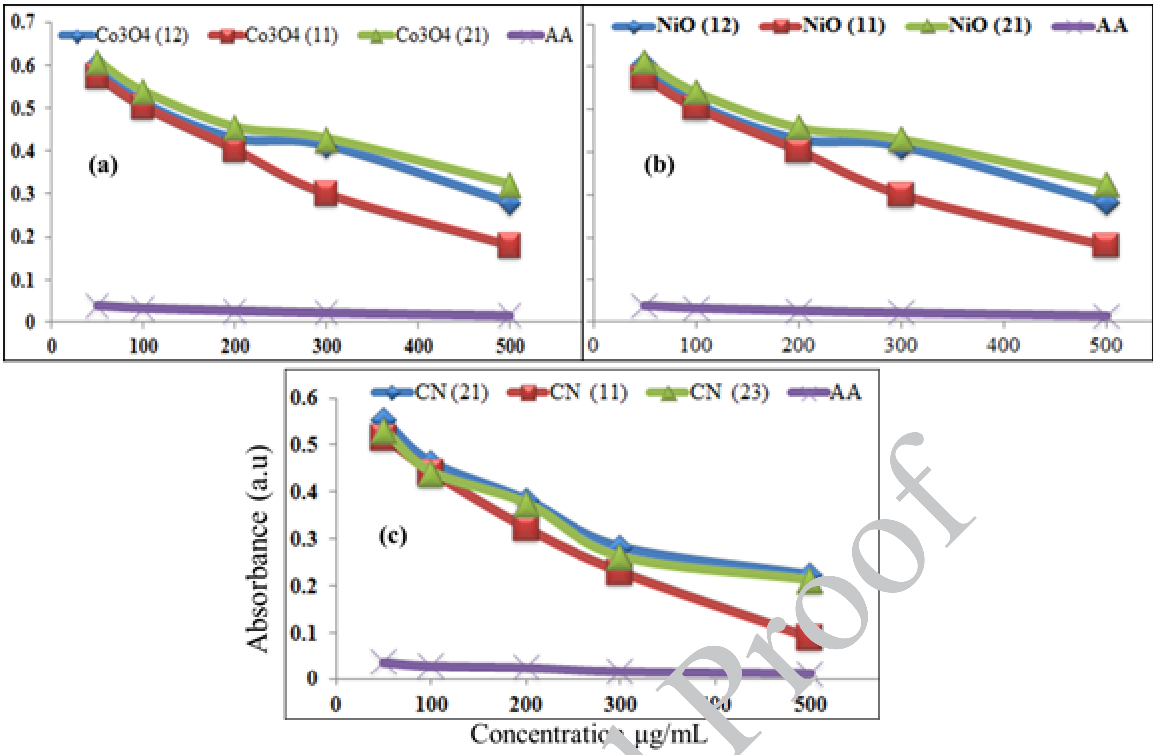

Fig. 19. The absorbance of (a) Co3O4 NPs, (b) NiO NPs, and (c) CN CSNs at concentrations of (50, 100, 200, 300, and 500 µg/mL).

and then the drug is targeted to the mitochondria and leads to cell death [66]

Antioxidant activities analysis result

The scavenging activity of *D. stramonium* leaf extract-mediated Co_3O_4 and NiO NPs, as well as CN CSNs, was tested against the stable free radical 2, 2-diphenyl-1-picrylhydrazyl (DPPH) using spectroscopic techniques. The antioxidant activity test of Co3O4 and NiO NPs, as well as CN CSNs at 50, 100, 200, 300, and 500 µg/mL concentrations, were determined The ability of these metal oxide nanoparticles to donate electrons is believed to be the basis for their effect on DPPH. The samples introduced into the solution reduce a violet DPPH to a yellow color depending on concentration. As shown in Fig. 19, the absorbance of the reaction mixture at 517 nm was measured using a spectrophotometer and displayed as a function of MONPs and CSN concentration.

The absorbance value reflects the level of DPPH reduction by Co_3O_4 and NiO NPs, as well as CN CSNs are used to assess their antioxidant activity. As depicted in Fig. 19, the absorbance of the reference medication (ascorbic acid), MONPs, and CSNs containing DPPH at 517 nm decreased as their concentration increased. The drop in absorbance suggests that the MONPs and CSNs are successfully neutralizing the DPPH free radical, validating their antioxidant activity. MONPs and CSNs have increased antioxidant action as their absorbance decreases. Furthermore, because of their significant band gap energy, MONPs with small sizes decrease absorbance quicker than those with large sizes. This ensured that the small-sized particles were powerful antioxidants. Furthermore, because of their high band gap energy, MONPs with small sizes lose absorbance more quickly than those with large sizes. This guaranteed that the small particles were effective antioxidants. Finally, as shown in Fig.s 19 (a, b, and c), the absorbance order of MONPs synthesized at three volume ratios is (21) > (12) > (11) and CSNs at (21) > (23) > (11) concentration ratios.

The percentage scavenging effect of Co_3O_4 and NiO NPs against DPPH was measured to determine their antioxidant activity. The percentage scavenging indicates the amount to which these MONPS scavenge the DPPH radicals. Fig. 20 (a) and Table 2 demonstrate that Co_3O_4 NPs produced in a (11) volume ratio inhibit 9.230, 22.564, 37.949, 53.846, and 63.308% at 50, 100, 200, 300,

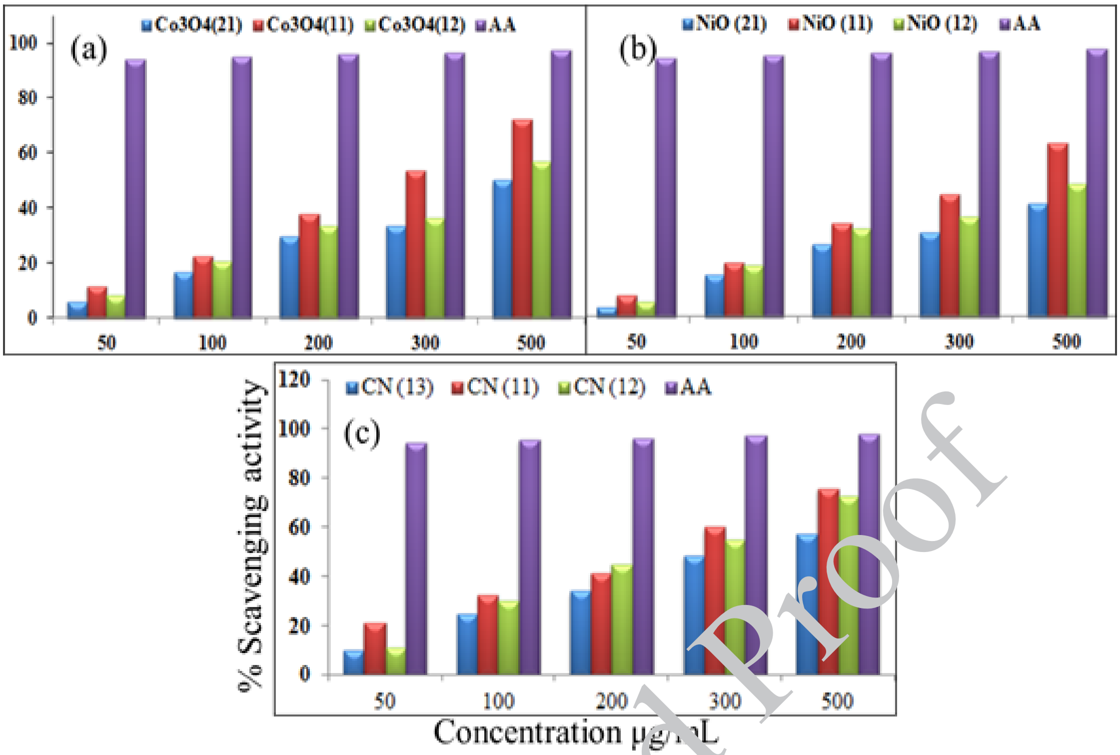

Fig. 20. The antioxidant activity of (a) Co3O4, (b) NiO, and (c) CN CSNs

and 500 μg/mL, respectively. As the concentration of Co3O4 NPs increases, so does their capacity to scavenge DPPH radicals. Additionally, the percentage scavenging of Co_3O_4 NPs synthesized in (12) was also found to be 4.103 (50), 15.385 (100), 28.205 (200), 36.410 (300), and 54.359% (500 μg/mL), whereas (21) scavenge 4.103 (50), 15.385 (100), 28.205 (200), 36.410 (300), and 54.359% (500 μg/mL). Among the three ratios, Co3O4 (11) NPs showed good scavenging potential against the DPPH radical. Similarly, the scavenging activity of NiO NPs was studied and their activity increases with concentration. The scavenging activity of NiO NPs synthesized in three volume ratios was raised in the order of (2:1), (1:2), and (1:1). At 500 μg/mL, Co_3O_4 (11) and NiO (11) NPs demonstrated scavenging activity about 63.308 and 57.0769%, respectively. Co_3O_4 NPs are commonly reported to have stronger antioxidant activity than NiO NPs. This is mostly due to the high redox potential of Co_3O_4 NPs. Co3O4 NPs with high redox potential are more likely to transfer electrons to DPPH, preventing oxidative damage.

Similarly, the antioxidant activity of CN CSNs was investigated as shown in Fig. 20(c) Table 2. The percentage scavenging activity of CN (11) at 50, 100, 200, 300, and 500 μg/mL was found to be 15.07, 26.35, 38.18, 56.29, and 65.98%. The result of the percentage scavenging activity achieved by CN CSNs was more than that of the parent material. The potent antioxidant activity of CSNs is believed to be due to the synergistic effect, redox potential, and surface area. The shell NiO NPs enhance the overall antioxidant of core-shell nanostructures which is a result due to the synergistic effects [31]. Similarly, the shell materials increase the core's redox potential and surface area, allowing for effective electron transport between the Co3O4 core and the NiO NPs shells, thus enhancing DPPH scavenging capabilities [67].

The IC_{50} values for DPPH radical scavenging activity of Co_3O_4 (11) NPs, NiO (11) NPs, CN11, and ascorbic acid were found to be 158.11, 165.62, 111.11, and 44.48 μg/mL, respectively. The CN11 with an IC_{50} of 111.11 μg/mL scavenged DPPH radicals by about 50%. This means the study shows that CN CSNs have a higher scavenging activity than individual Co_3O_4 and NiO NPs.

The mechanistic interaction of MONPs and CSNs with DPPH involves supplying electrons to the

Table 2. Percentage radical scavenging and IC_{50} of Co_3O_4, NiO NPs, and CN CSNs

Concentration (µg/mL)		50	100	200	300	500	IC_{50}
NPs	Ratios						(µg/mL)
Co_3O_4	2:1	4.102	13.333	29.744	33.846	47.589	262.21
	1:1	9.230	22.564	37.949	53.846	63.308	158.11
	1:2	4.103	15.385	31.205	36.410	54.359	239.34
NiO	2:1	3.589	15.385	26.666	30.769	41.538	290.01
	1:1	7.692	20.002	34.359	44.615	57.0769	165.62
	1:2	5.641	18.974	32.3077	36.410	4[illegible]18	275.62
CN	CN21	10.29	23.01	34.31	48.53	57.[illegible]2	130.61
	CN11	15.07	26.35	38.18	56.29	6[illegible].98	111.11
	CN23	9.27	20.93	31.09	44.91	[illegible]1.84	144.47
AA		94.154	95.077	96	96.769	97.846	44.84

DPPH radical, to reduce the nitrogen atom as seen in Fig. 21. According to the mechanism outlined by F. Rahman, the unstable purple-colored DPPH• solution was converted into a yellow stable DPPH reduced form during the DPPH• free-radical scavenging process [22, 68].

CONCLUSION

In this work, green synthesis was preferred to conventional techniques as it adopts a more ecologically conscious and sustainable method by embracing concepts of environmental responsibility. Co_3O_4 and NiO NPs as well as Co_3O_4@NiO CSNs were synthesized by green method utilizing their respective precursor salts and *Datura stramonium* plant leaf extract. The synthesis of the Co_3O_4, NiO NPs and Co_3O_4@NiO CSNs was confirmed by characterization techniques such as FTIR, UV-Vis, XRD, SEM-EDAX, TEM-HRTEM, and SAED. The Co_3O_4 NPs, NiO NPs, and CN CSNs became thermally stable at above 350, 380, and 400, respectively. This suggests that the core-shell architecture improves the thermal stability of the CN CSNs when compared

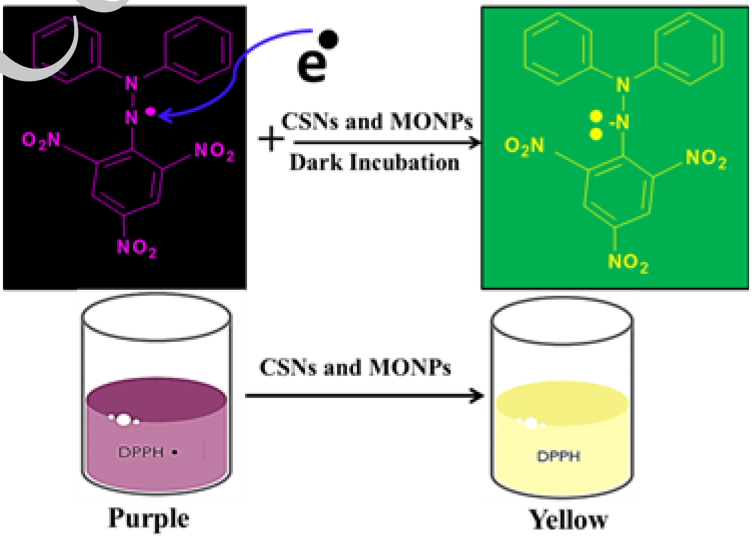

Fig. 21. Mechanistic interaction of electron of MONPs and CSNs against DPPH free radical molecule

to individual Co_3O_4 and NiO nanoparticles. The average crystalline size of CN21, CN11, and CN23 were 14, 13, and 16 nm, respectively. The number of Diffraction peaks in the shell material exceeds that of the core materials concerning the individual nanoparticles. This ensured that the NiO NPs were produced on the surface of Co_3O_4 NPs as a shell, consistent with prior results. The mean particle size of cubic CN CSNs obtained from the TEM image was 16.99 nm. Furthermore, the formation of CN CSNs was confirmed by miller indices obtained from SAED that correspond to the plane of core and shell particles. The cytotoxicity of green synthesized CN CSNs against breast cancer (MCF-7) cell lines at 12.5, 25, 50, 100, 200, 400, and 800 µg/mL exponential concentrations were 22.16, 32.20, 43.62, 52.41, 68.21, 74.11, and 81.38%, respectively. The results show that the percentage inhibition of CN CSNs on MCF-7 cell lines rises with increasing doses. The IC_{50} values for CN CSNs and Epirubicin on MFC-7 are 73.89 and 15.08, respectively, whereas on PBMC they are 455.86 and 419.40. The result evidenced that *D. stramonium* leaf extract-mediated CN CSNs have comparable anticancer activity against breast cancer (MCF-7) cell lines to the common medicines in use while being less hazardous to normal cells. To fully realize the promising .potentail of the Co_3O_4@NiO core-shell nanostructure in breast cancer treatment, future study that comprises cellular mechanistic interaction, further precursor optimization, and in-depth biological evaluation, might be needed.

DATA AVAILABILITY

The data used to support the study's findings are accessible from the relevant authors upon request.

ETHICAL APPROVAL

This article does not include any experiments with human participants or animals conducted by the authors.

CONFLICTS OF INTEREST

The authors state that they have no conflicts of interest.

FUNDING

The project was financed by the Ethiopian Ministry of Education (MoE)

AUTHORS' CONTRIBUTIONS

Gezahegn Tadesse, Prof. Tegene Desalegn, and Prof. H.C. Ananda Murthy were in charge of conceptualizing, designing the methodology, analyzing the data, and writing the manuscript. Lema Teshome and Addisalem Abebe contributed to the sample characterization process. All authors have read, revised, and provided feedback on the paper.

ACKNOWLEDGMENTS

The authors would like to acknowledge the Ethiopian Ministry of Education for its financial support, Adama Science and Technology University for its laboratory support, Research Centre, Research Institute of Materials Chemistry, Chungnam National University, Daejeon 34134, and Republic of Korea and Institute of Chemical Science, Indian Institute of Technology Mandi (IIT Mandi), H.P. India for characterization and biological activity test.

REFERENCES

1. Jha D, Thiruveedula PK, Pathak R, Kumar B, Gautam HK, Agnihotri S, Sharma AK, Kumar P. Multifunctional biosynthesized silver nanoparticles exhibiting excellent antimicrobial potential against multi-drug resistant microbes along with remarkable anticancerous properties. Materials Science and Engineering: C. 2017;80:659-69.
2. Al-Enazi NM, Alsamhary K, Kha M, Ameen F. In vitro anticancer and antibacterial performance of biosynthesized Ag and Ce co-doped ZnO NPs. Bioprocess Biosyst Eng [Internet]. 2023;46(1):89–103.
3. Siegel RL, Miller KD, Fuchs HE, Jemal A. Cancer statistics, 2022. CA Cancer J Clin. 2022;72(1):7–33.
4. Gwon K, Park JD, Lee S, Yu JS, Lee DN. Biocompatible Core–Shell-Structured Si-Based NiO Nanoflowers and Their Anticancer Activity. Pharmaceutics. 2022;14(2):268.
5. Osman Y, Elsharkawy T, Hashim TM, Alratroot JA, Aljindan F, Almulla L, et al. Study of Single Nucleotide Polymorphisms Associated with Breast Cancer Patients among Arab Ancestries. 2022;2022(1):2442109.
6. Gomathi AC, Xavier Rajarathinam SR, Mohammed Sadiq A, Rajeshkumar S. Anticancer activity of silver nanoparticles synthesized using aqueous fruit shell extract of Tamarindus indica on MCF-7 human breast cancer cell line. J Drug Deliv Sci Technol [Internet]. 2020;55:101376.
7. Abdelsattar AS, Kamel AG, Hussein AH, Azzam M, Makky S, Rezk N, et al. The Promising Antibacterial and Anticancer Activity of Green Synthesized Zinc

Nanoparticles in Combination with Silver and Gold Nanoparticles. J Inorg Organomet Polym Mater [Internet]. 2023;33(7):1868-81.

8. Hussain MM, Rahman MM, Asiri AM. Ultrasensitive and selective 4-aminophenol chemical sensor development based on nickel oxide nanoparticles decorated carbon nanotube nanocomposites for green environment. J Environ Sci (China) [Internet]. 2017;53(September 2018):27–38.
9. Sharifi M, Sharifi M, Jafari S, Hasan A, Hasan A, Paray BA, et al. Antimetastatic Activity of Lactoferrin-Coated Mesoporous Maghemite Nanoparticles in Breast Cancer Enabled by Combination Therapy. ACS Biomater Sci Eng. 2020;6(6):3574–3584.
10. Abdel-Fattah WI, W Ali G. On the anti-cancer activities of silver nanoparticles. J Appl Biotechnol Bioeng. 2018;5(1):43-46.
11. George BP, Rajendran NK, Houreld NN, Abrahamse H. Rubus Capped Zinc Oxide Nanoparticles Induce Apoptosis in MCF-7 Breast Cancer Cells. Molecules. 2022;27(20):6862.
12. Bahreyni A, Mohamud Y, Luo H. Emerging nanomedicines for effective breast cancer immunotherapy. J Nanobiotechnology [Internet]. 2020;18(1):1–14.
13. Tagde P, Najda A, Nagpal K, Kulkarni GT, Shah M, Ullah O, et al. Nanomedicine-Based Delivery Strategies for Breast Cancer Treatment and Management. Int J Mol Sci. 2022;23(5):2856.
14. Huang Y, Du Z, Bao G, Fang G, Cappadona M, McClements L, et al. Smart Drug-Delivery System of Upconversion Nanoparticles Coated with Mesoporous Silica for Controlled Release. Pharmaceutics. 2023;15(1):89.
15. D’Souza JN, Prabhu A, Nagaraja GK, Navada K M, Kouser S, Manasa DJ. Unravelling the human triple negative breast cancer suppressive activity of biocompatible zinc oxide nanostructures influenced by Vateria indica (L.) fruit phytochemicals. Mater Sci Eng C. 2021;122(January).
16. Pillai AM, Sivasankarapillai VS, Rahdar A, Joseph J, Sadeghfar F, A R, et al. Green synthesis and characterization of zinc oxide nanoparticles with antibacterial and antifungal activity. J Mol Struct. 2020;128107.
17. Ajarem JS, Maodaa SN, Allam AA, Taher MM, Khalaf M. Benign Synthesis of Cobalt Oxide Nanoparticles Containing Red Algae Extract: Antioxidant, Antimicrobial, Anticancer, and Anticoagulant Activity. J Clust Sci [Internet]. 2022;33(2):717–728.
18. Alarifi S, Ali D, Alkahtani S, Alhader MS. Iron oxide nanoparticles induce oxidative stress, DNA damage, and caspase activation in the human breast cancer cell line. Biol Trace Elem Res. 2014;159(1–3):416–424.
19. Abu-Serie MM, Eltarahony M. Novel nanoformulation of disulfiram with bacterially synthesized copper oxide nanoparticles for augmenting anticancer activity: an in vitro study. Cancer Nanotechnol [Internet]. 2021;12(1):1–17.
20. Kganyago P, Mahlaule-Glory LM, Mathipa MM, Ntsendwana B, Mketo N, Mbita Z, et al. Synthesis of NiO nanoparticles via a green route using Monsonia burkeana: The physical and biological properties. J Photochem Photobiol B Biol. 2018;182:18–26.
21. Lee KX, Shameli K, Nagao Y, Yew YP, Teow SY, Moeini H. Potential use of gold-silver core-shell nanoparticles derived from Garcinia mangostana peel for anticancer compound, protocatechuic acid delivery. Front Mol Biosci. 2022;9(October):1–15.
22. Orshiso TA, Zereffa EA, Murthy HCA, Demissie TB, Pardeshi O, Avhad LS, et al. Biosynthesis of Artemisia abyssinica Leaf Extract-Mediated Bimetallic ZnO-CuO Nanoparticles: Antioxidant, Anticancer, and Molecular Docking Studies. ACS Omega. 2023;8(44):41039–41053.
23. Alshehri AA, Malik MA. Biogenic fabrication of ZnO nanoparticles using Trigonella foenum-graecum (Fenugreek) for proficient photocatalytic degradation of methylene blue under UV irradiation. J Mater Sci Mater Electron [Internet]. 2019;30(17):16156–16173.
24. Wahab R, Siddiqui MA, Ahmad J, Saquib Q, Al-Khedhairy AA. Cytotoxic and molecular assessment against breast (MCF-7) cancer cells with cobalt oxide nanoballs. J King Saud Univ - Sci [Internet]. 2021;33(5):101467.
25. Shawki MM, Sadieque A El, Elabd S, Moustafa ME. Synergetic Effect of Tumor Treating Fields and Zinc Oxide Nanoparticles on Cell Apoptosis and Genotoxicity of Three Different Human Cancer Cell Lines. Molecules. 2022;27(14).
26. Sundram S, Baskar S, Subramanian A. Green synthesized nickel doped cobalt ferrite nanoparticles exhibit antibacterial activity and induce reactive oxygen species mediated apoptosis in MCF-7 breast cancer cells through inhibition of PI3K/Akt/mTOR pathway. Environ Toxicol. 2022;37(12):2877–2888.
27. Mahendra C, Chandra MN, Murali M, Abhilash MR, Singh SB, Satish S, et al. Phyto-fabricated ZnO nanoparticles from Canthium dicoccum (L.) for antimicrobial, anti-tuberculosis and antioxidant activity. Process Biochem. 2020;89:220–226.
28. Hemanth Kumar NK, Murali M, Satish A, Brijesh Singh S, Gowtham HG, Mahesh HM, et al. Bioactive and Biocompatible Nature of Green Synthesized Zinc Oxide Nanoparticles from Simarouba glauca DC.: An Endemic Plant to Western Ghats, India. J Clust Sci. 2020;31(2):523–534.
29. Khalil AT, Ovais M, Ullah I, Ali M, Shinwari ZK, Maaza M. Physical properties, biological applications and biocompatibility studies on biosynthesized single phase cobalt oxide (Co3O4) nanoparticles via Sageretia thea (Osbeck.). Arab J Chem. 2020;13(1):606–619.
30. Ramalingam V, Harshavardhan M, Dinesh Kumar S,

Malathi devi S. Wet chemical mediated hematite α-Fe2O3 nanoparticles synthesis: Preparation, characterization and anticancer activity against human metastatic ovarian cancer. J Alloys Compd. 2020;834:155118.
31. Zhang Y, Mahdavi B, Mohammadhosseini M, Rezaei-Seresht E, Paydarfard S, Qorbani M, et al. Green synthesis of NiO nanoparticles using Calendula officinalis extract: Chemical charactrization, antioxidant, cytotoxicity, and anti-esophageal carcinoma properties. Arab J Chem [Internet]. 2021;14(5):103105.
32. Alqarni LS, Alghamdi MD, Alshahrani AA, Nassar AM. Green Nanotechnology: Recent Research on Bioresource-Based Nanoparticle Synthesis and Applications. J Chem. 2022;2022:4030999.
33. Paul D, Mangla S, Neogi S. Antibacterial study of CuO-NiO-ZnO trimetallic oxide nanoparticle. Mater Lett [Internet]. 2020;271:127740.
34. Zhu CL, Chou SW, He SF, Liao WN, Chen CC. Synthesis of core/shell metal oxide/polyaniline nanocomposites and hollow polyaniline capsules. Nanotechnology. 2007;18(27):8–14.
35. Yang Q, Lu Z, Li T, Sun X, Liu J. Hierarchical construction of core-shell metal oxide nanoarrays with ultrahigh areal capacitance. Nano Energy [Internet]. 2014;7:170–8.
36. Sarani M, Hamidian K, Barani M, Adeli-Sardou M, Khonakdar HA. α-Fe2O3@Ag and Fe3O4@Ag Core-Shell Nanoparticles: Green Synthesis, Magnetic Properties and Cytotoxic Performance. ChemistryOpen. 2023;202200250:1–10.
37. Tadesse G, Ananda Murthy HC, Ravikumar CR, Naveen Kumar T, Teshome L, Desalegn T. In Situ Green Synthesis of Co3O4@ZnO Core-Shell Nanoparticles Using Datura stramonium Leaf Extract: Antibacterial and Antioxidant Studies. Bioinorg Chem Appl. 2023;2023(1):5019838.
38. Tamanis E, Sledevskis E, Ogurcovs A, Gerbreders V, Paskevics V. Synthesis of Core/Shell CuO-Zno Nanoparticles and Their Second-Harmonic Generation Performance. Latv J Phys Tech Sci. 2015;52(5):41–6.
39. Snezhkina AV, Kudryavtseva AV, Kardymon OL, Savvateeva MV, Melnikova NV, Krasnov GS, Dmitriev AA. ROS generation and antioxidant defense systems in normal and malignant cells. Oxid Med Cell Longev. 2019;2019(1):6175804.
40. Kelele KG, Murthy HCA, Balachandran R, Tadesse A, Nikodimos Y, Tufa LT, et al. Synthesis and characterization of Mo-doped barium strontium titanate nanopowder via slow injection sol–gel processing. Chem Pap [Internet]. 2023;77(1):129-139.41.
41. Yin X, Zhi C, Sun W, Lv LP, Wang Y. Multilayer NiO@Co3O4@graphene quantum dots hollow spheres for high-performance lithium-ion batteries and supercapacitors. J Mater Chem A. 2019;7(13):7800–7814.
42. Dinga E, Mthiyane DMN, Marume U, Botha TL, Horn S, Pieters R, et al. Biosynthesis of ZnO nanoparticles using Melia azedarach seed extract: Evaluation of the cytotoxic and antimicrobial potency. OpenNano [Internet]. 2022;8(June):100068.
43. Alharbi NS, Alsubhi NS, Felimban AI. Green synthesis of silver nanoparticles using medicinal plants: Characterization and application. J Radiat Res Appl Sci [Internet]. 2022;15(3):109–124.
44. Srivastava R. The Medicinal Significance of Datura stramonium: A Review. Biomed J Sci Tech Res. 2020;29(2):22223–22226.
45. Sharma M, Dhaliwal I, Rana K, Delta AK, Kaushik P. Phytochemistry, pharmacology, and toxicology of datura species—a review. Antioxidants. 2021;10(8):1–12.
46. Das S, Kumar P, Basu SP. Phytoconstituents and Therapeutic Potentials of Datura Stramonium Linn. J Drug Deliv Ther. 2012;2(3):4–7.
47. Khalil AT, Ovais M, Ullah I, Ali M, Shinwari ZK, Hassan D, et al. Sageretia thea (Osbeck.) modulated biosynthesis of NiO nanoparticles and their in vitro pharmacognostic, antioxidant and cytotoxic potential. Artif Cells, Nanomedicine Biotechnol [Internet]. 2018;46(4):838–852.
48. Anjum S, Nawaz K, Ahmad B, Hano C, Abbasi BH. Green synthesis of biocompatible core-shell (Au-Ag) and hybrid (Au-ZnO and Ag-ZnO) bimetallic nanoparticles and evaluation of their potential antibacterial, antidiabetic, antiglycation and anticancer activities. RSC Adv. 2022;12(37):23845–23859.
49. Bhardwaj K, Kumar S, Ojha S. Antioxidant activity and FT-IR analysis of Datura innoxia and Datura metel leaf and seed methanolic extracts. African J Tradit Complement Altern Med. 2016;13(5):7–16.
50. Bekele ET, Sintayehu YD, Murthy HCA, Shume MS, Ayanie GT, Turunesh DJ, et al. Synthesis of ZnO nanoparticles mediated by natural products of Acanthus sennii leaf extract for electrochemical sensing and photocatalytic applications: a comparative study of volume ratios. Chem Pap [Internet]. 2022;76(9):5967–5983.
51. Hussain S, Ali Muazzam M, Ahmed M, Ahmad M, Mustafa Z, Murtaza S, et al. Green synthesis of nickel oxide nanoparticles using Acacia nilotica leaf extracts and investigation of their electrochemical and biological properties. J Taibah Univ Sci [Internet]. 2023;17(1).
52. Zhao Y, Li K, Sheng B, Chen F, Song Y. Nitrogen-doped core-shell mesoporous carbonaceous nanospheres for effective removal of fluorine in capacitive deionization. Water (Switzerland). 2023;15(3):608.
53. Sanad MF, Meneses-Brassea BP, Blazer DS, Pourmiri S, Hadjipanayis GC, El-Gendy AA. Superparamagnetic fe/au nanoparticles and their feasibility for magnetic hyperthermia. Appl Sci. 2021;11(14).

54. Selvanathan V, Shahinuzzaman M, Selvanathan S, Sarkar DK, Algethami N, Alkhammash HI, et al. Phytochemical-assisted green synthesis of nickel oxide nanoparticles for application as electrocatalysts in oxygen evolution reaction. Catalysts. 2021;11(12):1523.
55. Vennela AB, Mangalaraj D, Muthukumarasamy N, Agilan S, Hemalatha K V. Structural and optical properties of Co 3 O 4 nanoparticles prepared by sol-gel technique for photocatalytic application. Int J Electrochem Sci. 2019;14(4):3535–52.
56. Aldeen TS, Ahmed Mohamed HE, Maaza M. ZnO nanoparticles prepared via a green synthesis approach: Physical properties, photocatalytic and antibacterial activity. J Phys Chem Solids [Internet]. 2022;160:110313.
57. Kim JC, Kim KJ, Lee SM. Preparation and characterization of core-shell structure hard carbon/si-carbon composites with multiple shell structures as anode materials for lithium-ion batteries. Energies. 2021;14(8):2104.
58. Nzilu DM, Madivoli ES, Makhanu DS, Wanakai SI, Kiprono GK, Kareru PG. Green synthesis of copper oxide nanoparticles and its efficiency in degradation of rifampicin antibiotic. Sci Rep [Internet]. 2023;13(1):1–18.
59. Li C, Wei A, Liu J, Xiao Z, Liu Z, Zhao Y. Synthesis of CoS@NiS core/shell nanoarrays as efficient counter electrode for dye-sensitized solar cells. J Mater Sci Mater Electron. 2017;28(6):4904–4907.
60. Cai T, Fang G, Tian X, Yin J, Chen C, Ge C. Optimization for Antibacterial Efficacy of Noble Metal-Based Core-Shell Nanostructures and Effect of Nature Organic Matter. 2019;13(11):12694-12702.
61. Liu S, Wei K, Cheng F, Li Y, Xue H. Ammonia Sensor Based on Co2+/SCN− Modified Core-Shell MCM-41 for Rapid Naked-Eye Colorimetric Detection. Chemosensors. 2023;11(6):336.
62. Rahman F, Majed Patwary MA, Bakar Siddique MA, Bashar MS, Haque MA, Akter B, et al. Green synthesis of zinc oxide nanoparticles using Cocos nucifera leaf extract: characterization, antimicrobial, antioxidant and photocatalytic activity. R Soc Open Sci. 2022;9(11):220858.
63. Ghasemian Dazmiri M, Alinezhad H, Hossaini Z, Bekhradnia AR. Green synthesis of Fe3O4/ZnO magnetic core-shell nanoparticles by Petasites hybridus rhizome water extract and their application for the synthesis of pyran derivatives: Investigation of antioxidant and antimicrobial activity. Appl Organomet Chem. 2020;34(9):1–13.
64. Raeisi M, Alijani HQ, Peydayesh M, Khatami M, Bagheri Baravati F, Borhani F, et al. Magnetic cobalt oxide nanosheets: green synthesis and in vitro cytotoxicity. Bioprocess Biosyst Eng. 2021;44(7):1423–1432.
65. Wingett D, Louka P, Anders CB, Zhang J, Punnoose A. A role of ZnO nanoparticle electrostatic properties in cancer cell cytotoxicity. Nanotechnol Sci Appl. 2016;9:29–45.
66. Wongrakpanich A, Joiner MA, Anderson ME, Salem AK. Mitochondria-targeting particles. 2014;9:2531–2543.
67. Iqbal J, Abbasi BA, Mahmood T, Hameed S, Munir A, Kanwal S. Green synthesis and characterizations of Nickel oxide nanoparticles using leaf extract of Rhamnus virgata and their potential biological applications. Appl Organomet Chem. 2019;33(8):e4950.
68. Ajarem JS, Maodaa SN, Allam AA, Taher MM, Khalaf M. Benign Synthesis of Cobalt Oxide Nanoparticles Containing Red Algae Extract: Antioxidant, Antimicrobial, Anticancer, and Anticoagulant Activity. J Clust Sci. 2021;1-2.